https://doi.org/10.5194/egusphere-2026-4451
Preprint. Discussion started: 22 September 2026

Major-Element Geochemistry, Redox Systematics, and Petrogenesis of the Estonian Rapakivi Intrusions, Finnish Wiborg Batholith, and Onas intrusion: A Revised Analysis of Fennoscandian AMCG Magmatism

Juan David Solano-Acosta*

Department of Geology, Tallinn University of Technology, Ehitajate tee 5, Tallinn, 19086, Estonia

Correspondence: Juan David Solano-Acosta* (jusola@ttu.ee)

Abstract. Rapakivi granitoids are a distinctive expression of Proterozoic intracontinental magmatism and provide constraints on crust–mantle interaction, lithospheric reworking, and the thermal evolution of stabilised continental crust. In Fennoscandia, the Wiborg suite is the earliest rapakivi-AMCG (anorthosite–mangerite–charnockite–granite) magmatic episode occurred at ∼1.65–1.62 Ga following the Svecofennian orogeny and is represented by broadly coeval intrusions in southern Finland and Estonia. Here, we integrate 186 whole-rock analyses from this older suite, including the Wiborg Batholith and the Taebla, Ereda, Neeme, Onas, Märjamaa, Kloostri, and Naissaare granites, together with the younger Riga Batholith (∼1.59 Ga) as a temporal and geochemical comparator. Major-element and iron-speciation data, $CIPW$ normative mineralogy, and thermobarometric proxies are used to test whether the older Fennoscandian rapakivi–AMCG suite records a common regional evolution or distinct magma-reservoir histories.The granitoids are predominantly high-K, ferroan, alkali-calcic to alkaline, and metaluminous to marginally peraluminous, but their major-element systematics define distinct intrusion- and phase-specific evolutionary trends rather than a uniform regional differentiation path. This compositional heterogeneity is also captured by centred log-ratio principal component analysis (CLR-PCA), in which the first two components account for 74.01% of the total variance. PC1 primarily contrasts relative enrichment in P_2O_5, TiO_2, and MgO with relative enrichment in SiO_2, K_2O, Na_2O, and Al_2O_3. Multiphase intrusions record internally systematic but contrasting evolutionary trajectories along these compositional gradients, including shifts towards more silicic and alkali-rich compositions and variable depletion of components associated with calcic plagioclase, Mg-bearing silicates, Fe-Ti oxides, and apatite. Hierarchical clustering similarly separates several evolved phases from their earlier counterparts, reinforcing the interpretation of phase-specific differentiation. These compositional differences are consistent with variable fractional crystallisation, locally modified by crystal accumulation, magma recharge, volatile evolution, and wall-rock assimilation. Ferroan indices and $Mg\#$ primarily record Fe-Mg fractionation, whereas $Fe^{3+}\#$ reveals non-monotonic, reservoir-dependent redox evolution. The resulting discordance between major-element affinity, normative oxide proportions, and ferric-iron speciation indicates that ferroan character and whole-rock oxidation state evolved only partly in tandem. Temperature proxies indicate crystallisation over approximately 620-900 °C, while most normative pressure estimates remain below ∼ 5 kbar, consistent with predominantly shallow- to mid-crustal emplacement. Collectively, the results indicate that these intrusions represent related but independently evolving A-type magma

https://doi.org/10.5194/egusphere-2026-4451
Preprint. Discussion started: 22 September 2026

reservoirs within the Fennoscandian rapakivi-AMCG system, whose contrasting compositions record local differentiation and redox histories superimposed on a shared post-orogenic tectono-magmatic framework.

1 Introduction

A-type granites are relatively dry, commonly ferroan felsic rocks emplaced mainly in post-orogenic to anorogenic settings and characterised by enrichment in alkalis, $HFSE$, $HREE$, Zr, Nb, and Ta, together with low concentrations of Co, Sc, Cr, Ni, Ba, Sr, and Eu (Loiselle and Wones, 1979; Eby, 1992; Frost and Frost, 1997; Frost et al., 2001; Vigneresse, 2005; Dall'Agnol and de Oliveira, 2007). Rapakivi granites constitute a distinctive A-type subtype, classically defined by rounded alkali-feldspar megacrysts that may be mantled by oligoclase in wiborgitic varieties or remain unmantled in pyterlitic varieties, although associated porphyritic, equigranular, and aplitic facies may lack the characteristic ovoid texture (Haapala and Rämö, 1992; Rämö and Haapala, 1995, 2005). In Fennoscandia, they are predominantly subsolvus monzogranites to syenogranites with high Fe/Mg, K/Na, and Ga/Al ratios, enrichment in most $REEs$, and negative Eu anomalies, whereas rapakivi-type granitoids elsewhere may extend to quartz-syenitic and locally peralkaline compositions (Haapala, 1995; Vigneresse, 2005; Bonin, 2007; Heinonen et al., 2010b, a; Valkama et al., 2016; Dall'Agnol et al., 2012; Solano-Acosta, 2026). Their isotopic signatures generally indicate substantial crustal input, commonly accompanied by interaction with mantle-derived mafic magmas (Larin, 2009; Heinonen et al., 2010b; Sharkov, 2010; Rämö et al., 2014; Solano-Acosta et al., 2025a, 2026).

Rapakivi granites are particularly abundant in Precambrian cratons and have been documented across Baltica, Laurentia, Amazonia, and other ancient continental domains (Puura and Flodén, 1996, 1999, 2000; Bogdanova et al., 2006, 2015; Sharkov, 2010; Salminen et al., 2021; Grabarczyk et al., 2023; Hinchey et al., 2024). Rapakivi-like granitoids have also been described in Phanerozoic belts, although their petrogenetic equivalence to the classical Precambrian suites remains debated (Rajesh, 2000; Christiansen et al., 2007; Luo et al., 2024). In Fennoscandia, rapakivi granites constitute the felsic component of Palaeo- to early Mesoproterozoic Anorthosite-Mangerite-Charnockite-Granite (AMCG) associations, which may also contain massif-type anorthosites, gabbros, mangerites, ferrodioritic dykes, and related mafic rocks (Haapala and Rämö, 1992; Rämö and Haapala, 1995, 2005; Dall'Agnol and de Oliveira, 2007). This magmatism was concentrated mainly between ca. 1.7-1.5 Ga, with an important peak at $\sim$ 1.6 Ga during the Nuna-Columbia supercontinent cycle (Salminen et al., 2021; Johansson et al., 2022). Although younger AMCG activity continued until $\sim$ 1.0 Ga, equivalent younger episodes are not recognised in Fennoscandia (Emslie, 1978; Frost et al., 1999; Vigneresse, 2005; Christiansen et al., 2007; Hinchey et al., 2024).

The development of Fennoscandian AMCG suites has been related to thermal perturbation of the continental lithosphere, mantle upwelling, mafic underplating, and partial melting of lower-crustal sources (Bonin, 2007; Kukkonen and Lauri, 2009; Sharkov, 2010; Salminen et al., 2021; Johansson, 2023). Classical models emphasise intracontinental extension, crustal thinning, and listric faulting as the principal mechanisms responsible for magma generation and emplacement (Emslie, 1978; Korja et al., 1993, 2001; Sharkov, 2010). However, the absence of extensive coeval sedimentary basins, the prolonged duration of AMCG activity, and the lack of systematic age progression among individual complexes are difficult to reconcile with a single rift or migrating-hotspot model (Hoffman, 1989; Ashwal and Bybee, 2017; Salminen et al., 2021; Mitchell et al., 2021).

https://doi.org/10.5194/egusphere-2026-4451
Preprint. Discussion started: 22 September 2026

Alternative interpretations invoke mantle superswells, asthenospheric upwelling, thermal insulation beneath Nuna-Columbia, and repeated reactivation of inherited Svecofennian structures (Trubitsyn et al., 2003; Pirajno and Santosh, 2015; Salminen et al., 2021; Solano-Acosta et al., 2025a). Under these conditions, mafic underplating and crustal melting could have generated compositionally contrasting magmas, while pre-existing shear zones and strike-slip corridors controlled their ascent and emplacement (Branigan, 1987; Elo and Korja, 1993; Grocott et al., 1999; Puura and Flodén, 1999, 2000; All et al., 2006; Larin, 2009; Nordbäck et al., 2024).

The southern Finnish mainland, the Åland archipelago, the Gulf of Finland, Estonia, Latvia, and adjacent areas of Russia form the classical Fennoscandian rapakivi province (Fig.1a). Fennoscandian rapakivi granites are commonly grouped into four principal age-defined suites: the Wiborg Suite (1.65-1.62 Ga), the Åland-Riga Suite (1.59-1.56 Ga), the Salmi Suite (1.55-1.53 Ga), and the Ragunda Suite (1.53-1.47 Ga) (Rämö et al., 1996; Ahl, 1997; Puura and Flodén, 2000; Salminen et al., 2021; Grabarczyk et al., 2023). The Wiborg Suite represents the earliest of these major magmatic episodes and extends across southeastern Finland and Russian Karelia. Covering more than 20,000 km^2, the Wiborg rapakivi region comprises the Wiborg Batholith and several associated or satellite intrusions, including Suomenniemi, Ahvenisto, Bodom, Obbnäs, and Onas, as well as mafic and locally anorthositic rocks (Ahl, 1997; Puura and Flodén, 1999). These complexes were emplaced into Palaeoproterozoic crust and contain multiple intrusive phases distinguished by lithology, age, and local gravity and magnetic characteristics (Elo and Korja, 1993; All et al., 2006; Solano-Acosta et al., 2025a). The broadly coeval rapakivi granitoids of northern Estonia represent smaller and predominantly concealed components of this early Fennoscandian magmatic episode.

In Estonia, the crystalline basement and its rapakivi intrusions are concealed beneath $\sim$ 150-800 m of Neoproterozoic and Palaeozoic sedimentary rocks. Their distribution and subsurface geometry have therefore been reconstructed principally from drilling, seismic observations, and potential-field datasets (Korja et al., 1993; Puura and Flodén, 1996, 1999, 2000; All et al., 2006; Bogdanova et al., 2006, 2015; Solano-Acosta et al., 2023). The Estonian rapakivi granitoids include the Märjamaa intrusion and its Kloostri satellite, Naissaare, Taebla, Neeme, and Ereda, together with the substantially larger and younger Riga Batholith farther south (Fig.1b) (Soesoo and Niin, 1992; Klein et al., 1994; Rämö et al., 1996; Kirs et al., 2004). The northern Estonian bodies are mainly pink, medium- to coarse-grained monzogranites and syenogranites, locally accompanied by porphyritic, aplitic, and microsyenitic phases. Although classic plagioclase-mantled alkali-feldspar ovoids are uncommon, their petrographic, geochemical, geochronological, and isotopic characteristics establish an affinity with the Wiborg Suite (Soesoo and Niin, 1992; Klein et al., 1994; Rämö et al., 1996; Ahl, 1997; Rämö and Haapala, 2005). The younger Riga Batholith is associated with a distinct magmatic episode and is part of the subsequent second AMCG Suite.

Inherited Svecofennian structures likely controlled the emplacement of rapakivi intrusions in Finland and Estonia. A NW-SE transtensional strike-slip system across southern Finland and Estonia is associated with major fracture networks, deformation zones, and present-day seismicity (Nordbäck et al., 2024; Solano-Acosta et al., 2023; Soosalu et al., 2022) (Figs. 1a,b), where Rapkaivi intrusions normally occur near reactivated shear corridors, fault intersections, and crustal discontinuities (Branigan, 1987; Salminen et al., 2021; Nordbäck et al., 2024). Märjamaa-Kloostri and Naissaare lie close to the NW-trending Åland-Paldiski-Pskov Deformation Zone (PPDZ), whereas the Riga massif is associated with the Middle Estonian Fault Zone (MEFZ), indicating structural control on magma ascent and intrusion geometry (Solano-Acosta et al., 2023, 2025a).

https://doi.org/10.5194/egusphere-2026-4451
Preprint. Discussion started: 22 September 2026

This study presents the first phase-resolved comparison of major-element compositions across the Wiborg-suite rapakivi granitoids, including the Wiborg, Taebla, Ereda, Neeme, Onas, Märjamaa-Kloostri, and Naissaare intrusions. A unified set of geochemical classifications, compositional statistical analyses, and whole-rock thermobarometric proxies is applied to the concealed Estonian bodies and the Finnish Wiborg and Onas intrusions. The study evaluates compositional variability among the individual bodies and magmatic phases, with emphasis on differentiation trends, ferroan affinity, redox systematics, and petrogenetic relationships. It determines whether the Estonian intrusions preserve a coherent geochemical signature within the broader Wiborg-suite AMCG system or record distinct reservoir-scale magmatic histories.

2 Geological setting

2.1 Regional tectonic framework

Baltica, northeast of the Trans-European Suture Zone, comprises the Archean-Proterozoic Fennoscandian, Volgo-Uralian, and Sarmatian crustal domains (Fig.1a). Their progressive assembly involved crustal accretion, arc magmatism, and basin closure between ca. 2.1 and 1.79 Ga (Gorbatschev and Bogdanova, 1993; Terentiev and Santosh, 2020; Wang et al., 2020; Johansson et al., 2022). Within Fennoscandia, the Svecofennian orogeny (SO) incorporated successive island arcs and microcontinents, including the Bergslagen and Livonia blocks, and culminated in the 1.84-1.79 Ga Svecobaltic collision (Nironen, 1997; Nironen et al., 2000; Lahtinen et al., 2005; Bogdanova et al., 2006, 2015; Nironen, 2017; Johansson et al., 2022; Solano-Acosta et al., 2025b). Orogenic collapse and crustal stabilisation followed at $\sim$ 1.79-1.77 Ga, while the final linkage between Fennoscandia and Sarmatia was completed by ca. 1.70 Ga (Bogdanova et al., 2006, 2015; Johansson et al., 2022). Juvenile crust continued to accrete along the western margin of Baltica during the 1.73-1.48 Ga Gothian orogeny (Bogdanova et al., 2008, 2015; Nironen, 2017).

The resulting Fennoscandian crust consists of Archean nuclei bordered and locally reworked by Palaeoproterozoic mobile belts (Korsman et al., 1999; Korhonen et al., 2002; Lahtinen et al., 2005). Its southern part is characterised by obliquely oriented lithotectonic blocks and crustal-scale deformation zones that continue beneath the Baltic Sea and form the host framework for the younger rapakivi granitoid intrusions (Kukkonen and Lauri, 2009; Johansson et al., 2022; Nordbäck et al., 2024; Solano-Acosta et al., 2025a).

2.2 Estonian basement architecture

The Estonian crystalline basement consists principally of Palaeoproterozoic metamorphic and igneous assemblages intruded by younger Mesoproterozoic granitoids. Six structural-petrological zones are recognised: Tallinn, Alutaguse, Jõhvi, Tapa, West-Estonian, and South-Estonian (Fig.1b). These domains are distinguished by their lithological, metamorphic, geochemical, gravity, and magnetic characteristics (All et al., 2004; Bogdanova et al., 2015; Soesoo et al., 2020; Solano-Acosta et al., 2023).

https://doi.org/10.5194/egusphere-2026-4451
Preprint. Discussion started: 22 September 2026

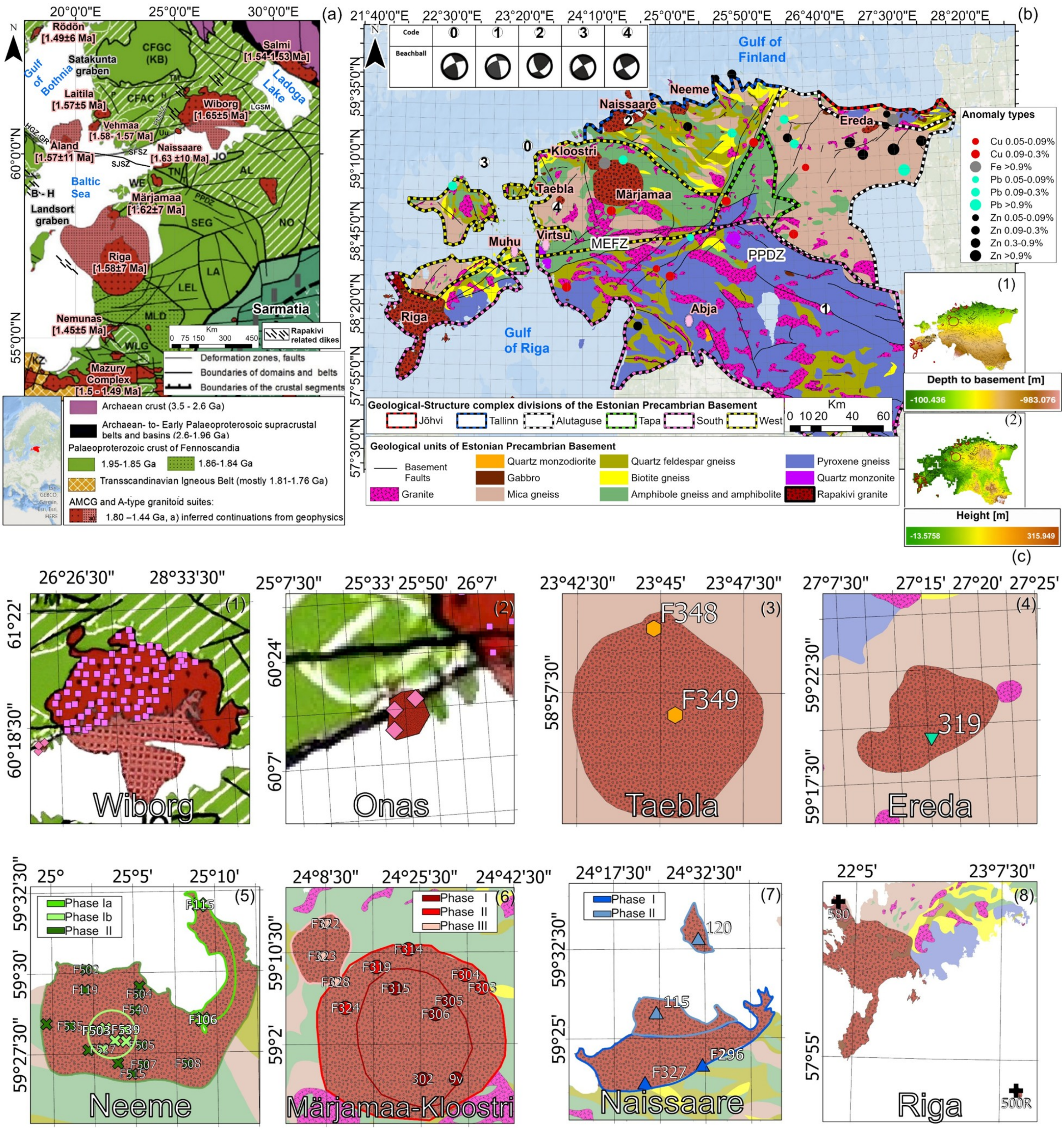

https://doi.org/10.5194/egusphere-2026-4451
Preprint. Discussion started: 22 September 2026

Figure 1. Geological setting of the study zone. **(a)** Major Paleoproterozoic tectonic domains of Fennoscandia, modified after Bogdanova et al. (2015), highlighting the most prominent rapakivi bodies, with the Märjamaa and Kloostri granitoids study area marked by a red rectangle. The white diagonal ruling over the greenish area indicates Svecofennian sedimentary basins. The abbreviations are AL - Alutaguse, B-H - Breven-Hällefors dike swarms, CFAC - Central Finland Arc Complex, CFGC - Central Finland Granitoid Complex, H - Häme belt, HGZ-GR - Hagsta-Gävle-Rättvik Zone, JO - Jõhvi, KB - Keitele microcontinent, LA - Latgalia, LEL - Latvian-East Lithuanian, LGSM - Late Svecofennian Granite-Migmatite zone, MLD - Mid-Lithuanian domain, NO - Novgorod - P - Pirkanmaa belt, SEG - South Estonian granulite domain, T - Tapa, TN - Tallinn, TM - Tampere belt, Uu - Uusimaa belt, WE - West Estonian domain, WLG - West Lithuanian granulite domain. Shear and fault zones are abbreviated as follows: MEFZ - Middle Estonian Fault Zone, PMSZ - Porkkala-Mäntsälä Shear Zone, PPDZ - Paldiski-Pskov Deformation Zone, SFSZ - South Finland Shear Zone, and SJSZ - Sottunga-Jurmo Shear Zone. Age rapakivi granitoids of Fennoscandia are constrained from Laitakari et al. (1996); Ahl (1997); Rämö et al. (1996); Skridlaitė et al. (2007); Larin (2009); Sharkov (2010); Soesoo and Hade (2012); Johansson et al. (2016); Grabarczyk et al. (2023). **(b)** Precambrian geological map of the Estonian basement. The upper-left inset shows the distribution of granulite- and amphibolite-facies metamorphic rocks after Bogdanova et al. (2015). Geological information, and (1) depth-to-basement (DTB) and (2) topographic data, were obtained from the Land Board Geoportal of the Republic of Estonia (https://xgis.maaamet.ee/xgis2/page/app/geoloogia400k). The epicentres of earthquakes analysed by Soosalu et al. (2022) are shown as black dots labelled with a number (code), each with its respective focal mechanism, enhancing the transpressional tectonic system (Solano-Acosta et al., 2023, 2025a). **(c)** Locations of the analysed rapakivi samples, including GTK data from the Finnish (1) Wiborg and (2) Onas bodies (Rasilainen et al., 2007), and drill-core samples from the Estonian intrusions (3–8) (Kivisilla et al., 1999). The Neeme, Märjamaa-Kloostri, and Naissaare intrusions are superimposed on the corresponding plutonic phases as defined by Klein et al. (1994).

The Tallinn and Alutaguse domains are dominated by amphibolite-facies metavolcanic and metasedimentary assemblages and correlate with the Uusimaa arc and associated back-arc successions in southern Finland. Their development has been linked to double-subduction systems, arc amalgamation, and closure of Palaeoproterozoic oceanic basins at $\sim$ 1.87 Ga (All et al., 2004; Soesoo et al., 2004; Kukkonen and Lauri, 2009; Bogdanova et al., 2015; Nironen, 2017; Solano-Acosta et al., 2025b). The West-Estonian domain consists predominantly of high-grade metasedimentary and metaigneous rocks affected by granulite-facies metamorphism, whereas the South-Estonian domain contains orthogneisses and mafic-felsic granulites (Puura et al., 2004; Soesoo et al., 2004, 2006, 2020).

The domains are separated by major basement discontinuities. The NW-SE-trending PPDZ separates the northern and eastern crustal blocks from the western and southern domains, whereas the $\sim$ E-W trending MEFZ juxtaposes basement blocks with contrasting metamorphic characteristics (All et al., 2004; Puura et al., 2004; Bogdanova et al., 2015). Regional gravity and magnetic anomalies trace these structures northwestward beneath the Baltic Sea towards the Sottunga-Jurmo Shear Zone and related deformation corridors in southern Finland and Sweden (Korhonen et al., 2002; Bogdanova et al., 2006; Högdahl et al., 2009; Bogdanova et al., 2015; Korja and Kosonen, 2015; Soosalu et al., 2022; Nordbäck et al., 2024).

Geochronological evidence shows that the majority of the Estonian basement, formed between $\sim$ 1.92 and 1.76 Ga, is part of the Svecofennian crust. This interval encompasses the North Estonian metavolcanics ($\sim$1.92 Ga), granulite-facies metavolcanics in southern Estonia ($\sim$1.83-1.82 Ga), and tonalitic intrusions in the Tapa region ($\sim$1.82 Ga) (Petersell and Levchenkov, 1994; Soesoo et al., 2004, 2006; Kirs et al., 2009; Bogdanova et al., 2015). Zircon $U-Pb$ dating of magnetite-bearing gneisses from the Jõhvi belt yields ages of $\sim$1.87-1.79 Ga (Soesoo et al., 2020). A younger assemblage comprises tonalites, charnockites, and orthopyroxene-garnet gneisses in southern Estonia, which crystallised between $\sim$1.79 and 1.76 Ga, while gabbro-norite dykes in the area record ages of $\sim$1.77 Ga (Soesoo et al., 2004, 2006).

https://doi.org/10.5194/egusphere-2026-4451
Preprint. Discussion started: 22 September 2026

2.3 Wiborg suite and chronologically related intrusions

The Wiborg Batholith is a polyphase composite intrusion emplaced mainly between ca. 1650 and 1625 Ma, with prominent age clusters near 1640 and 1630 Ma (Suominen, 1991; Vaasjoki et al., 1991; Rämö et al., 2014) (Fig.1c1). The best-constrained plutonic ages range from 1646 ± 4 Ma for fayalite-bearing hornblende granite along its northern flank to 1627 ± 3 Ma for dark wiborgite in its southern part, whereas a quartz-feldspar porphyry dyke dated at 1615 ± 6 Ma records younger subvolcanic activity. The batholith also contains associated granitic porphyries, gabbroic and anorthositic rocks, and hypabyssal mafic dykes (Ahl, 1997; Puura and Flodén, 2000). The smaller intrusions are described below according to their nominal crystallisation ages, while recognising their substantial temporal overlap with the polyphase evolution of Wiborg.

The Taebla body intrudes at ca. 1.648 Ga (Soesoo and Hade, 2012) (Fig.1c3). It is the smallest recognised rapakivi intrusion in northern Estonia, with a diameter of about 6 to 7 km. The intrusion is relatively homogeneous and primarily consists of leucocratic granite (Soesoo and Niin, 1992; Klein et al., 1994; Laitakari et al., 1996).

The Ereda intrusion records two reported age groups at ~ 1.642 and 1.627 Ga (Soesoo and Hade, 2012) (Fig.1c4). It forms an elongated body $\sim 15 \times 5$ km in size and consists predominantly of homogeneous porphyritic granite (Soesoo and Niin, 1992; Soesoo, 1993; Klein et al., 1994). A distinctive feature of the pluton is weak late- to post-magmatic deformation (Laitakari et al., 1996). Quartz constitutes $\sim 30-35\%$ of the rock and occurs in two generations. Microcline accounts for $\sim 35-45\%$ and forms tabular crystals and large, compositionally zoned phenocrysts reaching $3-4$ cm in diameter. Plagioclase occurs as euhedral tabular to prismatic crystals of andesine composition, whereas biotite constitutes $\sim 5-10\%$ and is locally altered to chlorite. Accessory phases include fluorite, apatite, zircon, epidote, rutile, magnetite, and hematite (Laitakari et al., 1996; Raukas and Teedumäe, 1997).

The Neeme intrusion, dated at ~ 1.63 Ga (Soesoo and Hade, 2012), forms a 25×20 km pluton partly extending beneath the Gulf of Finland (Fig.1c5). It consists of coarse- to medium-grained pinkish-grey porphyritic granite cut by aplites and microsyenites. Two melanocratic, locally granodioritic bodies in its central and northeastern parts define Phases Ia and Ib, whereas the remaining intrusion is more leucocratic; partially assimilated gneiss xenoliths and local trachytic fabrics also occur (Soesoo and Niin, 1992; Klein et al., 1994). The rocks contain quartz (20-25%), microcline (35-45%), oligoclase-andesine plagioclase (15-25%), and biotite (2-10%), with subordinate hornblende and muscovite. Accessory phases include apatite, fluorite, titanite, zircon, epidote, and opaque minerals (Puura and Flodén, 1996).

The Onas intrusion (Fig.1c2), situated along the southern Finnish coast, has a reported U-Pb zircon age of 1630 ± 10 Ma (Laitala, 1984; Laitakari et al., 1996), whereas its associated porphyry dykes yield an age of 1636 ± 6 Ma (Tornroos, 1984). Although the nominal age of the porphyry dykes is slightly older than that of the granite, the two ages overlap within uncertainty, and both rock types have been interpreted as products of the same magmatic system. The porphyry and diabase dykes occupy the same joint system, indicating that felsic and mafic dyke emplacement occurred within a closely spaced interval. The association of granitic units with granitic porphyry and basaltic hypabyssal dykes records multiple, temporally related stages of magma emplacement (Ahl, 1997; Puura and Flodén, 2000). The age of Onas broadly overlaps with that of Neeme, Märjamaa, and other northern Estonian bodies.

https://doi.org/10.5194/egusphere-2026-4451
Preprint. Discussion started: 22 September 2026

The Märjamaa-Kloostri system is the largest northern Estonian rapakivi intrusion, forming an asymmetrically rounded 40×25 km composite pluton within the West-Estonian domain (Fig.1c6) (All et al., 2004; Kirs et al., 2004; Solano-Acosta et al., 2023). Three phases are distinguished petrographically, geochemically, and geophysically (Klein et al., 1994; Solano-Acosta et al., 2025a, 2026). Earlier U–Pb zircon analyses of Phase I material from drill core 302 yielded upper-intercept ages of 1626 ± 13 Ma (Rämö et al., 1996). Subsequent dating produced a more precise age of 1626 ± 3 Ma for Phase I material from drill core 305 and an age of 1629.7 ± 4.2 Ma for Phase III material from the Kloostri drill core F323 (Potagin, 2024). Phase I is a central melanocratic granodiorite containing abundant gneiss xenoliths; Phase II is a peripheral, K-feldspar-rich biotite-hornblende granite; and Phase III is the northwestern Kloostri Na-rich leucogranite, characterised by albite, minor muscovite and fluorite, and local trachytoid fabric (Soesoo and Niin, 1992; Klein et al., 1994; Laitakari et al., 1996). The rocks contain quartz (20-30%), microcline and plagioclase (each 20-40%), and biotite (2-10%); hornblende is restricted to Phases I-II, while magnetite, ilmenite, zircon, apatite, titanite, fluorite, and epidote occur as accessory phases (Soesoo and Niin, 1992; Raukas and Teedumäe, 1997).

The Naissaare intrusion has an upper-intercept U-Pb zircon age of 1624 ± 10 Ma from Phase I material in drill core 327 (Rämö et al., 1996). The pluton extends partly beneath the Gulf of Finland and comprises porphyritic granite cut by aplite and microsyenite veins. It is divided into two compositionally distinct phases: peripheral melanocratic granite containing sporadic hornblende and central leucocratic granite with local trachytoid fabric, post-magmatic muscovite and fluorite, and petrographic similarities to the Kloostri leucogranite (Soesoo and Niin, 1992; Klein et al., 1994). The rocks contain quartz $(25-35\%)$, microcline $(35-45\%)$, oligoclase plagioclase $(20-25\%)$, and biotite, with apatite, titanite, zircon, epidote, magnetite, and ilmenite as accessory phases.

In addition to the rapakivi granitoids, the Estonian basement contains several small monzonitic to granodioritic intrusions with shoshonitic affinity, including Taadikvere, Muhu, Abja, and Virtsu. The partly gneissic Taadikvere granodiorite and Muhu quartz monzonite yield ages of ~ 1.83 Ga, whereas the Abja quartz monzonite and Virtsu intrusion are considerably younger, with reported U-Pb zircon ages of 1.638 Ga and 1606 ± 17 Ma, respectively (Soesoo and Hade, 2012). Despite their different emplacement ages, the Muhu, Abja, and Virtsu rocks display broadly similar shoshonitic and A-type geochemical affinities, while some high-K varieties from Muhu and Virtsu are compositionally comparable to Finnish rapakivi granites (Laitakari et al., 1996; Raukas and Teedumäe, 1997; Kirs et al., 2004; Soesoo and Hade, 2012).

The Riga Batholith, include it Estonian samples, is located on the islands of Saaremaa and Ruhnu. forms the southern part of the Riga-Åland-Bothnia rapakivi subprovince and comprises both silicic and mafic rocks that are petrographically and geochemically comparable to the principal components of Fennoscandian rapakivi-anorthosite associations (Puura and Flodén, 1999; Rämö et al., 1996; Puura and Flodén, 2000). U-Pb zircon ages of 1584 ± 7 Ma for biotite-hornblende granite and 1576 ± 2 Ma for olivine leucogabbronorite indicate broadly contemporaneous felsic and mafic magmatism within analytical uncertainty (Rämö et al., 1996). Geophysical interpretations further suggest that the batholith's emplacement was accompanied by substantial crustal thinning, estimated at ~ 10 km (Puura and Flodén, 1999; Korja et al., 2001; Puura and Flodén, 2000). Riga, therefore, represents a younger magmatic episode than the Wiborg-related bodies and is included in this study only as a limited regional comparator.

https://doi.org/10.5194/egusphere-2026-4451
Preprint. Discussion started: 22 September 2026

3 Materials and Methods

Whole-rock major-element data for the Estonian Precambrian basement have traditionally been obtained through wet-chemical analysis of drill-core samples (Kivisilla et al., 1999). The Estonian compilation used in this study includes SiO_2, TiO_2, Al_2O_3, Fe_2O_3, FeO, MnO, MgO, CaO, Na_2O, K_2O, P_2O_5, S_{tot}, and LOI, reported in wt.%. Data were compiled for the Märjamaa-Kloostri, Ereda, Taebla, Naissaare, Neeme, and Riga bodies. The analytical catalogue is publicly available through *GEOkirjandus*, where the corresponding analytical and sample records are archived in the SARV Geological Information System. The sampled drill cores can be located through the public Estonian Geological Survey dashboard.

Comparative Finnish data were extracted from the whole-rock geochemical database of the Geological Survey of Finland (GTK) compiled by Rasilainen et al. (2007). The database contains 6544 georeferenced samples and is distributed in Esri File Geodatabase and MS Excel formats through the GTK metadata service and the GTK Hakku portal. Samples assigned to the Wiborg Batholith and Onas intrusion were selected spatially in ArcGIS. The GTK records report the principal major-element oxides and total iron as FeO_{tot} but do not include LOI or separate (FeO, Fe^{2+}) and (Fe_2O_3, Fe^{3+}) concentrations.

The final compilation comprises 186 whole-rock analyses, including 102 samples from Estonia and 84 from Finland (Fig. 1c). The Estonian dataset includes Märjamaa Phase I ($n = 22$), Märjamaa Phase II ($n = 15$), Kloostri Phase III ($n = 10$), Neeme Phase Ia ($n = 10$), Neeme Phase Ib ($n = 10$), Neeme Phase II ($n = 17$), Naissaare Phase I ($n = 5$), Naissaare Phase II ($n = 2$), Ereda ($n = 3$), Taebla ($n = 5$), and Riga ($n = 3$), whereas the Finnish dataset comprises Wiborg ($n = 81$) and Onas ($n = 3$). Samples were grouped by intrusion and, where supported by geological information, assigned to individual magmatic phases using published petrographic, geochemical, and geophysical interpretations (Soesoo and Niin, 1992; Soesoo, 1993; Klein et al., 1994; Solano-Acosta et al., 2025a). The results and discussion follow an approximate age-based order, beginning with the Wiborg Batholith and continuing through Taebla, Ereda, Neeme, Onas, Märjamaa-Kloostri, and Naissaare of the Wiborg Suite, followed by the younger Riga Batholith of the Åland-Riga Suite. This order is used as an organisational framework rather than as a strictly resolved chronological sequence because the Wiborg Batholith records prolonged polyphase magmatism and several age estimates overlap (e.g., Rämö et al., 2014; Heinonen et al., 2017).

Iron speciation was standardised before major-element normalisation. For samples in which FeO and Fe_2O_3 were reported separately, the original analytical values were retained. For the GTK samples, which report only FeO_{tot}, FeO and Fe_2O_3 were estimated following the whole-rock ferric-ferrous partitioning procedure of Yang et al. (2021). This method estimates the ferric-iron proportion ($Fe^{3+}\#$) using whole-rock composition and zircon-saturation temperature for each granite sample. Zirconium concentrations were therefore required for the GTK samples and are reported in the Supplementary Material. The calculations were performed using the calculation spreadsheet of Yang et al. (2021).

Because iron speciation was not determined using a uniform analytical method across the complete compilation, the reconstructed Fe^{2+}/Fe^{3+} ratios are model-dependent. They were therefore used to assess relative Fe-Mg systematics and redox-related differences among the sample groups rather than to derive absolute oxygen-fugacity conditions. This limitation is particularly relevant when comparing measured iron speciation in the Estonian dataset with modelled values for the Finnish samples (Frost and Frost, 1997; Vigneresse, 2005; Dall'Agnol and de Oliveira, 2007; Sharkov, 2010; Yang et al., 2021).

https://doi.org/10.5194/egusphere-2026-4451
Preprint. Discussion started: 22 September 2026

Following iron standardisation, all analyses were recalculated on an anhydrous basis using SiO_2, TiO_2, Al_2O_3, Fe_2O_3, FeO, MnO, MgO, CaO, Na_2O, K_2O, and P_2O_5. These oxides were normalised to 100 $wt.\%$, while LOI and S_{tot} were excluded to remove variability associated with volatile components and permit direct comparison between the Estonian and GTK datasets. Total iron expressed as ferric iron was calculated as $Fe_2O_{3\text{tot}} = Fe_2O_3 + (1.111 \times FeO)$, and total iron expressed as ferrous iron as $FeO^* = 0.8998 \times Fe_2O_{3\text{tot}}$. Original LOI and S_{tot} values were retained in the compiled database for reference, where available.

Normative mineral proportions were calculated using the updated Cross-Iddings-Pirrson-Washington ($CIPW$) norm implemented in the Python-based *webNORM* application (Buckle et al., 2023), available at https://webnorm.streamlit.app/. The calculation follows the procedure of Verma et al. (2003) and applies the plutonic-rock iron correction of Le Maitre (1976). Because the $CIPW$ norm represents an idealised anhydrous mineral assemblage (Kelsey, 1965), it does not reproduce hydrous minerals such as biotite and hornblende observed in the rapakivi granitoids (Klein et al., 1994; Soesoo, 1993). Normative values were therefore used only to compare bulk compositional trends and the relative proportions of quartz, feldspars, Fe-Ti oxides, and phosphate phases, rather than as estimates of modal mineralogy. Normative pyroxene components, including enstatite-ferrosilite, clinoenstatite-clinoferrosilite, and diopside, as well as corundum, were retained in the calculations but were not interpreted as direct evidence of observed mineral assemblages (Andersson and Eklund, 1994; Eklund and Shebanov, 1999a, b; Rämö and Haapala, 2005).

3.1 Statistical methods

3.1.1 Compositional data preparation

The compositional analysis included SiO_2, TiO_2, Al_2O_3, FeO^*, MnO, MgO, CaO, Na_2O, K_2O, and P_2O_5. Separate FeO and Fe_2O_3 values were not included together with FeO^* to avoid redundant representation of total iron. All variables were screened for missing, non-finite, zero, and negative values. No invalid or non-positive values were identified; therefore, all 186 analyses were retained, and no zero replacement was required.

The selected oxide concentrations were first closed to a constant sum of 100 wt.% and then transformed using the centred log-ratio (CLR) transformation (Aitchison, 1982; Egozcue et al., 2024). The CLR transformation expresses each oxide relative to the geometric mean of the complete composition and reduces covariance effects associated with closure. The transformed dataset was checked for finite values and numerical consistency. Data-preparation diagnostics and the CLR-transformed values are provided in Tables S1-S2.

3.1.2 Compositional principal-component analysis

Principal-component analysis (PCA) was performed directly on the CLR-transformed major-element dataset (Aitchison, 1983; Filzmoser et al., 2009; Egozcue et al., 2024; Templ and Hofer, 2025). No additional unit-variance standardisation was applied, thereby preserving the relative geometry of the CLR-transformed compositions.

https://doi.org/10.5194/egusphere-2026-4451
Preprint. Discussion started: 22 September 2026

PCA scores and loadings were used to identify the principal relative major-element associations and to compare compositional variability among the rapakivi bodies and magmatic phases. Group centroids were calculated as the mean PCA scores for samples assigned to each body or phase and used to visualise the phase trajectories of the Neeme, Märjamaa-Kloostri, and Naissaare systems. Eigenvalues, explained variance, loadings, scores, and group centroids are reported in Tables S3-S4.

3.1.3 Hierarchical clustering of CLR phase centroids

Mean CLR compositions were calculated for each rapakivi body or magmatic phase. Euclidean distances among these centroids were then evaluated using agglomerative hierarchical clustering with Ward's linkage (Ward, 1963; Murtagh and Legendre, 2014). The analysis used all ten CLR-transformed major-element variables and was intended to complement the two-dimensional PCA projection by summarising similarities in complete relative major-element composition (Table S5).

Dendrogram proximity was interpreted solely as compositional similarity, not as evidence of a shared magma source, contemporaneity, or a direct genetic relationship. All compositional preprocessing, PCA, centroid calculations, and hierarchical clustering were conducted in Python using *NumPy*, *pandas*, *scikit-learn*, and *SciPy*.

3.2 Whole-rock compositional thermobarometry

Following the approach applied by Solano-Acosta et al. (2026), we derived theoretical pressure and temperature estimates from whole-rock major-element data and corresponding normalised $CIPW$ normative parameters.

Crystallisation pressures were obtained using the normative quartz and alkali-feldspar barometers of Yang (2017): $P_{Qz} = -0.2426 \times Qtz^3 + 26.392 \times Qtz^2 - 980.74 \times Qtz + 12563$ and $P_{Ab+Or} = 0.2426 \times (Ab+Or)^3 - 46.397 \times (Ab+Or)^2 + 2981.3 \times (Ab+Or) - 64224$, where P is expressed in MPa and Qtz, Ab, and Or are the normalised $CIPW$ normative proportions. The two barometers were applied separately because they yield closely matching pressure estimates for granitic compositions ($R^2 \approx 0.9$; Yang, 2017).

Whole-rock temperature proxies were calculated using the formulations of Duan et al. (2022), whom criticised zircon-saturation thermometry for magma temperature estimates, arguing that Zr exerts only a minor control on whole-rock chemistry, even though this method has been employed in rapakivi studies (e.g., Grabarczyk et al. (2023)). Instead, they proposed two equations for granitoids: $T_{SiO_2}[^\circ C] = -14.16 \times SiO_2[wt.\%] + 1723$ and $T_{MgO}[^\circ C] = 887.6 \times (MgO[wt.\%])^{0.0989}$, which approximate the temperatures of melt–crystal aggregates prior to complete solidification (Duan et al., 2022). These expressions characterise the thermal state of melt–crystal mixtures before solidification and provide an alternative to zircon-saturation thermometry, whose suitability for whole-rock compositions has been questioned as Zr contributes little to bulk-rock chemistry (Duan et al., 2022).

The calculated pressures and temperatures were used to compare the intrusive bodies and to assess them against published mineral-based constraints (Klein et al., 1994; Sharkov, 2010; Rämö et al., 2014). These estimates are proxies from whole-rock compositions, not substitutes for thermobarometric determinations based on measured mineral equilibria (Eklund et al., 1994; Andersson and Eklund, 1994; Klein et al., 1994; Elliott, 2001; Sharkov and Bogina, 2006).

https://doi.org/10.5194/egusphere-2026-4451
Preprint. Discussion started: 22 September 2026

4 Results

4.1 Major elemental trends

The major-element statistical data for each rapakivi body and its corresponding phase are summarised in Table 1 and the elemental relations in the Table 2. The distribution of the major element compositions is illustrated in Figure 2. The comparison tests whether these bodies define a common regional differentiation series or instead record distinct evolutionary pathways within separate magma reservoirs.

SiO_2 distributions indicate mainly felsic compositions but differ in dispersion. Wiborg spans the widest range ($\sim$ 65–78 $wt.\%$ SiO_2), consistent with its polyphase nature; Taebla and Onas each form a narrow cluster near 72 $wt.\%$. Ereda is shifted towards higher silica. In Neeme, Phases Ia and Ib have similar central values, but Phase Ib is more heterogeneous ($\sim$ 66–76 $wt.\%$), whereas Phase II is more silica-rich and restricted. In the Märjamaa-Kloostri system, SiO_2 increases systematically from Märjamaa Phase I through Phase II to Kloostri Phase III, defining the clearest phase-related trend. Naissaare Phases I and II largely overlap, and Riga occupies an intermediate, moderately dispersed range.

Al_2O_3 varies less systematically than SiO_2 and largely overlaps among bodies and phases. Wiborg, Onas, Märjamaa Phase I, and the Naissaare phases are comparatively Al-rich, whereas Ereda and Riga are Al-poor. In Neeme, Phase Ia has a narrow intermediate range, Phase Ib is most variable ($\sim$ 11–16 $wt.\%$), and Phase II is slightly lower. Across the Märjamaa-Kloostri system, Al_2O_3 decreases only slightly from Phase I to Phase III. Naissaare Phase II is marginally more Al-rich than Phase I, but their ranges overlap.

TiO_2 shows the clearest differentiation contrasts. Wiborg covers a broad range and exceeds 1 $wt.\%$, whereas Taebla and Ereda are lower and narrower. In Neeme, Phase Ia has moderate TiO_2, Phase Ib is slightly richer and more variable, and Phase II is distinctly depleted. Onas is homogeneous and Ti-poor. Märjamaa Phase I is the most Ti-rich in Estonia, with values exceeding 1 $wt.\%$, followed by a strong decrease in Märjamaa Phase II and Kloostri Phase III. Naissaare Phase I is slightly more Ti-rich than Phase II, and Riga is intermediate.

Measured FeO exceeds measured Fe_2O_3 in most bodies and phases, whereas $Fe_2O_{3,\mathrm{tot}}$ and FeO^* provide equivalent expressions of total whole-rock iron. Wiborg shows the broadest total-iron range, with FeO^* extending from $\sim$ 0.9 to 7.4 $wt.\%$, whereas Taebla is comparatively restricted and has nearly balanced average ferric and ferrous iron contents. Ereda is strongly ferrous dominated, with an average FeO of $\sim$ 3.1 $wt.\%$ compared with only 0.3 $wt.\%$ Fe_2O_3. Within Neeme, Phase Ib is the most Fe-rich and variable, reaching $\sim$ 6.9 $wt.\%$ FeO^*, whereas Phase II has the lowest average total iron. Onas is homogeneous and ferrous-dominated. In the Märjamaa-Kloostri system, total iron decreases from Märjamaa Phase I to Kloostri Phase III; however, Kloostri Phase III differs from the earlier phases in having average Fe_2O_3 slightly higher than FeO. Naissaare Phase I contains slightly more total iron than Phase II. Riga is the clearest ferric-dominated end-member, with an average Fe_2O_3 of $\sim$ 4.0 $wt.\%$ compared with 1.3 $wt.\%$ FeO, and reaches some of the highest total-iron values in the dataset.

MnO remains low throughout the dataset and broadly follows the distribution of total iron. Wiborg and Taebla show limited variability, whereas Ereda is consistently Mn poor. Within Neeme, Phase Ia has a restricted distribution, Phase Ib is more variable, and Phase II remains uniformly low. Onas is compositionally homogeneous. Märjamaa Phase I shows the greatest

https://doi.org/10.5194/egusphere-2026-4451
Preprint. Discussion started: 22 September 2026

Rapakivi body		N	SiO_2	TiO_2	Al_2O_3	Fe_2O_3	FeO	MnO	MgO	CaO	Na_2O	K_2O	P_2O_5	LOI	$Fe_2O_{3,tot}$	FeO^*	S_{tot}	SO_3
Wiborg	**Wiborg (Avg)**	81	71.29	0.5	13.66	1.06	2.68	0.06	0.31	1.83	2.98	5.5	0.13		4.03	3.63	0.01	0.03
	Wiborg (Min)		65.37	0.01	11.28	0.2	0.67	0.02	0.09	0.67	2.42	3.66	0.02		0.94	0.85	0.01	0.02
	Wiborg (Max)		78.26	1.15	15.09	1.93	5.71	0.12	0.87	3.65	3.61	6.47	0.5		8.27	7.44	0.03	0.07
Taebla	**Taebla (Avg)**	5	71.98	0.29	12.96	1.59	1.71	0.06	0.44	2.3	2.5	6.11	0.06	0.99	3.48	3.13	0.11	0.27
	Taebla (Min)		71.18	0.1	12.37	0.84	1.46	0.04	0.12	1.66	2.24	5.63	0.04	0.8	2.66	2.4	0.01	0.02
	Taebla (Max)		72.72	0.46	13.67	2.06	2.02	0.08	0.58	2.55	2.81	6.49	0.08	1.23	4.26	3.84	0.15	0.37
Ereda	**Ereda (Avg)**	3	74.22	0.29	11.76	0.33	3.14	0.02	0.6	1.78	2.15	5.62	0.08	0.95	3.82	3.44	0.03	0.07
	Ereda (Min)		71.52	0.2	10.97	0.19	2.31	0.01	0.31	1.34	2.01	5.03	0.04	0.87	2.99	2.69	0.01	0.02
	Ereda (Max)		76.24	0.4	12.25	0.55	4.65	0.04	0.85	2.29	2.24	6.06	0.12	1.06	5.36	4.82	0.05	0.12
Neeme	**Neeme Ia (Avg)**	10	71.17	0.41	13.52	1.32	2.19	0.05	0.79	2.66	2.73	5.04	0.14	0.86	3.75	3.37	0.11	0.28
	Neeme Ia (Min)		68.26	0.31	12.69	1.08	1.9	0.03	0.37	2.09	1.98	3.62	0.12	0.49	3.26	2.94	0.05	0.12
	Neeme Ia (Max)		72.3	0.57	14.62	1.54	3.17	0.07	1.63	3.33	3.28	5.92	0.2	1.18	5.01	4.51	0.14	0.35
	Neeme Ib (Avg)	10	71.28	0.45	13.44	0.98	2.6	0.07	0.87	2.28	2.8	5.04	0.17	0.77	3.88	3.49	0.12	0.3
	Neeme Ib (Min)		66.23	0.21	11.33	0.5	1.24	0.03	0.4	1.51	2.23	2.94	0.06	0.57	2.13	1.92	0.09	0.22
	Neeme Ib (Max)		76.47	0.9	16.23	1.78	5.35	0.12	1.44	3.56	4.26	6.04	0.38	1.08	7.72	6.94	0.17	0.42
	Neeme II (Avg)	17	74.61	0.21	12.78	0.96	1.41	0.05	0.46	1.66	2.57	5.22	0.06	0.69	2.52	2.27	0.1	0.25
	Neeme II (Min)		72.55	0.05	11.74	0.28	0.43	0.03	0.09	1.07	1.38	4.16	0.02	0.2	1.51	1.36	0.09	0.22
	Neeme II (Max)		76.22	0.33	14.23	1.53	2.19	0.06	0.7	2.16	3.48	6.43	0.11	1.25	3.4	3.06	0.14	0.35
Onas	**Onas (Avg)**	3	72.07	0.29	13.73	0.95	2.29	0.07	0.21	1.33	3.19	5.84	0.03		3.5	3.15	0.01	0.02
	Onas (Min)		71.28	0.27	13.26	0.95	2.21	0.07	0.15	1.25	3.08	5.73	0.03		3.41	3.07	0.01	0.02
	Onas (Max)		72.94	0.3	14.13	0.97	2.38	0.08	0.3	1.37	3.28	5.93	0.03		3.61	3.25	0.01	0.02
Märjamaa -Kloostri	**Märjamaa I (Avg)**	22	67.48	0.79	13.72	2.32	2.77	0.09	1.31	3.16	2.84	5.19	0.33	0.7	5.4	4.86	0.11	0.27
	Märjamaa I (Min)		64.44	0.1	12.64	0.35	0.76	0.01	0.4	1.36	2.33	4.38	0.01	0.35	1.2	1.08	0.03	0.07
	Märjamaa I (Max)		74.74	1.12	14.39	3.83	3.71	0.28	1.86	4.94	3.33	6.35	0.5	1.29	7.29	6.56	0.22	0.55
	Märjamaa II (Avg)	15	70.44	0.4	13.52	1.06	2.69	0.07	0.65	2.03	2.61	6.4	0.11	0.63	4.05	3.65	0.09	0.23
	Märjamaa II (Min)		67.04	0.17	11.98	0.29	1.09	0.03	0.38	1.02	2.41	4.68	0.02	0.22	1.51	1.35	0.09	0.22
	Märjamaa II (Max)		74.38	0.74	15.91	2.56	4.64	0.13	1.28	3.28	2.85	7.74	0.38	1.43	6.63	5.97	0.1	0.25
	Kloostri III (Avg)	10	72.19	0.33	13.27	1.38	1.2	0.07	0.61	1.96	3.37	5.6	0.04	0.47	2.71	2.43	0.09	0.22
	Kloostri III (Min)		70.44	0.08	12.32	0.69	0.32	0.01	0.22	1.35	2.83	3.9	0.01	0.28	1.05	0.95	0.09	0.22
	Kloostri III (Max)		75.75	0.64	14.	2.49	1.93	0.13	1.08	2.66	4.7	6.3	0.08	0.69	4.64	4.17	0.09	0.22
Naissaare	**Naissaare I (Avg)**	5	71.03	0.31	13.63	1.48	2.05	0.03	0.71	2.03	2.18	6.43	0.11	0.96	3.76	3.38	0.09	0.22
	Naissaare I (Min)		67.13	0.26	12.32	0.93	1.67	0.03	0.49	1.71	2.03	5.74	0.06	0.82	2.87	2.58	0.09	0.22
	Naissaare I (Max)		72.91	0.35	15.29	2.26	2.77	0.05	0.95	2.85	2.38	7.44	0.25	1.36	5.33	4.8	0.09	0.22
	Naissaare II (Avg)	2	71.5	0.27	13.87	1.05	2.04	0.02	0.41	1.34	2.76	6.62	0.11	0.96	3.31	2.98	0.06	0.14
	Naissaare II (Min)		70.09	0.22	13.51	0.43	1.96	0.01	0.28	1.33	2.47	5.97	0.07	0.93	2.78	2.5	0.02	0.05
	Naissaare II (Max)		72.91	0.32	14.24	1.67	2.11	0.04	0.55	1.35	3.04	7.27	0.15	0.98	3.84	3.46	0.09	0.22
Riga	**Riga (Avg)**	3	71.32	0.45	12.27	3.96	1.29	0.03	0.74	0.8	2.17	6.77	0.21	1.08	5.4	4.86	0.06	0.15
	Riga (Min)		68.3	0.25	11.82	2.48	0.37	0.02	0.25	0.66	1.9	4.63	0.07	0.6	3.34	3.	0.05	0.12
	Riga (Max)		73.06	0.6	12.74	5.22	2.73	0.04	1.71	1.03	2.57	7.88	0.44	1.85	8.26	7.43	0.07	0.17

Table 1. Average, minimum, and maximum major-element compositions $[wt.\%]$ for each intrusion and magmatic phase. The complete sample-level dataset is provided in the Supplementary Material. Rapakivi bodies are grouped by intrusion, drill core, and magmatic phase, as shown in Figure 1c. Only fresh to slightly altered silicate-rock analyses with original, non-normalised major-element totals of $100 \pm 1.5\ wt.\%$ and $LOI < 3\ wt.\%$ were retained. Selected analyses were recalculated to $100\ wt.\%$ on an anhydrous basis. Total iron was expressed as $Fe_2O_{3\mathrm{tot}} = Fe_2O_3 + 1.111, FeO$ and $FeO^* = 0.8998, Fe_2O_{3\mathrm{tot}}$. Sulfur was converted to SO_3 equivalent using $SO_3[wt.\%] = S[wt.\%] \times (80.07/32.07)$.

dispersion, with individual values approaching $0.3\ wt.\%$, followed by lower distributions in Märjamaa Phase II and Kloostri Phase III. Naissaare Phase I contains slightly more MnO than Phase II, whereas Riga remains uniformly low.

MgO, CaO, and $Mg\#$ broadly distinguish the less evolved from the more differentiated groups. Wiborg is generally Mg poor, while Taebla and Ereda occupy somewhat higher MgO and $Mg\#$ intervals. Within Neeme, Phase Ia contains moderately elevated MgO and CaO, Phase Ib is slightly richer in MgO and occupies the highest $Mg\#$ interval within the intrusion, and Phase II is depleted in both oxides. Onas is the most Mg-poor group and occupies the lowest $Mg\#$ interval. Märjamaa Phase I is the most Mg- and Ca-rich Estonian group, with CaO locally approaching $5\ wt.\%$. Both oxides decrease markedly in Märjamaa Phase II and remain low in Kloostri Phase III. The partial increase in $Mg\#$ from Phase II to Phase III reflects a stronger decline in FeO^* than in MgO rather than renewed Mg enrichment. Naissaare Phase I is richer in MgO and CaO

https://doi.org/10.5194/egusphere-2026-4451
Preprint. Discussion started: 22 September 2026

Rapakivi body		Geochemical Relations																			CIPW after Buckle et al. (2023)						
		K_2O/Na_2O	FeO^*/MgO	$Mg\#$	A/NK	ASI	Na_2O+K_2O	$FeO^*/(FeO^*+MgO)$	Fe_2O_3/FeO	$Fe\#$	X_{Mag}	$MALI$	T_{SiO_2}	T_{MgO}	$P_{Qz,MPa}$	$P_{Ab-Or,MPa}$	$P_{Qz,kbar}$	$P_{Ab-Or,kbar}$	**DF1**	**DF2**	Qtz	An	Ab	Or	Ap	Ilm	Mag
Wiborg	**Wiborg (Avg)**	1.86	13.14	12.61	1.26	0.97	8.48	0.92	0.4	0.29	0.74	6.65	713.47	780.55	247.91	260.63	2.48	2.61	-1.18	-0.15	28.36	7.36	25.18	32.48	0.31	0.95	2.53
	Wiborg (Min)	1.25	5.79	6.91	1.15	0.88	6.6	0.85	0.29	0.22	0.66	2.95	614.83	700.37	10.45	0.83	0.1	0.01	-2.24	-3.88	21.97	2.67	20.47	21.6	0.05	0.02	0.6
	Wiborg (Max)	2.45	24.	23.55	1.62	1.18	9.22	0.96	0.46	0.32	0.97	8.09	797.4	875.44	435.41	450.62	4.35	4.51	0.36	0.39	41.68	14.91	30.54	38.22	1.16	2.18	4.53
Taebla	**Taebla (Avg)**	2.45	9.11	19.05	1.21	0.87	8.62	0.88	0.92	0.47	0.81	6.31	703.77	808.45	209.72	222.82	2.1	2.23	-2.95	-1.01	28.94	6.06	21.19	36.14	0.14	0.55	2.22
	Taebla (Min)	2.25	5.92	8.29	1.18	0.83	8.1	0.86	0.51	0.34	0.75	5.75	693.29	720.64	130.57	142.42	1.31	1.42	-3.42	-1.63	27.63	5.34	18.96	33.27	0.09	0.19	1.76
	Taebla (Max)	2.73	19.72	23.14	1.25	0.94	9.13	0.95	1.23	0.55	0.9	7.47	715.11	840.87	267.22	281.14	2.67	2.81	-2.29	-0.79	31.14	7.1	23.77	38.35	0.19	0.87	2.69
Ereda	**Ereda (Avg)**	2.61	6.3	23.38	1.22	0.92	7.78	0.85	0.13	0.11	0.81	6.	672.03	837.79	175.8	180.91	1.76	1.81	1.09	0.46	35.34	5.83	18.2	33.19	0.19	0.54	2.35
	Ereda (Min)	2.5	4.21	16.51	1.19	0.85	7.04	0.81	0.04	0.04	0.8	4.75	643.48	790.99	22.4	32.44	0.22	0.32	-0.53	-0.11	30.01	5.46	17.	29.71	0.09	0.38	1.84
	Ereda (Max)	2.7	9.01	29.73	1.25	0.98	8.31	0.9	0.24	0.19	0.83	6.65	710.21	873.33	350.13	343.13	3.5	3.43	2.73	0.96	40.31	6.05	18.92	35.74	0.28	0.76	3.35
Neeme	**Neeme Ia (Avg)**	1.88	4.74	28.45	1.37	0.92	7.77	0.82	0.61	0.38	0.75	5.11	715.25	861.22	192.4	203.05	1.92	2.03	-1.56	-1.08	29.37	9.32	23.09	29.78	0.33	0.77	2.26
	Neeme Ia (Min)	1.1	2.76	17.55	1.15	0.81	6.26	0.73	0.47	0.32	0.71	3.53	699.29	805.	82.03	92.98	0.82	0.93	-2.23	-1.84	25.43	4.53	16.75	21.39	0.28	0.59	1.97
	Neeme Ia (Max)	2.4	8.37	39.21	1.71	1.05	8.74	0.89	0.74	0.42	0.79	6.2	756.48	931.6	318.67	311.49	3.19	3.11	-0.17	-0.46	35.75	13.79	27.74	34.98	0.46	1.08	2.84
	Neeme Ib (Avg)	1.88	3.99	31.18	1.34	0.95	7.84	0.8	0.43	0.29	0.74	5.56	713.64	870.98	204.33	211.93	2.04	2.12	-0.81	-0.23	29.49	8.62	23.68	29.78	0.39	0.85	2.34
	Neeme Ib (Min)	0.69	3.11	26.85	1.14	0.86	6.9	0.76	0.21	0.18	0.69	3.64	640.15	809.76	5.51	4.17	0.06	0.04	-2.38	-1.47	20.46	3.89	18.87	17.36	0.14	0.4	1.34
	Neeme Ib (Max)	2.58	4.86	36.45	1.59	1.07	8.71	0.83	0.79	0.44	0.79	7.	785.12	920.	489.85	505.34	4.9	5.05	1.1	0.49	38.05	16.01	36.01	35.67	0.88	1.71	4.46
	Neeme II (Avg)	2.15	5.57	25.94	1.31	1.	7.79	0.83	0.8	0.41	0.8	6.13	666.48	816.39	181.35	186.15	1.81	1.86	-2.22	-0.99	35.3	6.54	21.74	30.86	0.14	0.4	1.54
	Neeme II (Min)	1.5	3.68	10.58	1.1	0.87	6.41	0.79	0.19	0.16	0.75	4.53	643.68	699.67	21.01	31.03	0.21	0.31	-4.74	-3.55	29.12	3.12	11.68	24.57	0.05	0.1	0.97
	Neeme II (Max)	4.68	15.07	32.66	1.56	1.21	9.32	0.94	2.4	0.71	0.91	7.94	695.64	857.23	715.43	710.05	7.15	7.1	0.12	0.69	41.85	10.06	29.45	38.01	0.26	0.63	2.12
Onas	**Onas (Avg)**	1.83	16.	10.54	1.19	0.98	9.02	0.94	0.42	0.29	0.81	7.7	702.5	758.3	310.18	324.39	3.1	3.24	-1.64	0.65	27.52	5.89	26.98	34.45	0.07	0.55	2.3
	Onas (Min)	1.81	10.97	8.22	1.18	0.98	8.81	0.92	0.41	0.29	0.8	7.56	690.11	737.7	216.16	229.45	2.16	2.29	-1.75	0.45	25.55	5.43	26.05	33.85	0.07	0.51	2.21
	Onas (Max)	1.86	19.9	13.98	1.2	0.99	9.21	0.95	0.43	0.3	0.82	7.85	713.66	786.93	404.62	419.65	4.05	4.2	-1.52	0.76	29.72	6.31	27.74	35.02	0.07	0.57	2.39
Märjamaa -Kloostri	**Märjamaa I (Avg)**	1.84	3.78	32.46	1.34	0.86	8.03	0.79	0.86	0.45	0.7	4.87	767.47	906.55	418.7	433.34	4.19	4.33	-1.89	-1.16	23.21	9.3	24.03	30.67	0.75	1.51	3.25
	Märjamaa I (Min)	1.51	2.69	23.56	1.07	0.72	6.71	0.73	0.27	0.21	0.58	2.89	664.71	810.81	105.06	116.43	1.05	1.16	-4.17	-3.46	17.67	2.37	19.72	25.89	0.02	0.19	0.8
	Märjamaa I (Max)	2.43	5.78	39.89	1.65	0.97	9.21	0.85	1.63	0.62	0.87	7.81	810.54	943.61	1138.65	1156.12	11.39	11.56	-0.68	0.48	29.91	14.3	28.17	37.54	1.16	2.13	4.28
	Märjamaa II (Avg)	2.45	5.75	24.79	1.21	0.91	9.01	0.84	0.41	0.28	0.78	6.98	725.6	846.1	464.07	478.56	4.64	4.79	-1.42	0.17	25.66	6.05	22.07	37.8	0.26	0.76	2.6
	Märjamaa II (Min)	1.77	3.2	15.05	1.06	0.81	7.32	0.76	0.26	0.21	0.72	4.04	669.75	807.43	125.63	137.38	1.26	1.37	-2.57	-0.95	18.04	2.14	20.38	27.62	0.05	0.32	1.05
	Märjamaa II (Max)	2.79	10.07	35.77	1.42	1.05	10.54	0.91	0.8	0.44	0.86	8.55	773.74	909.8	1430.27	1448.26	14.3	14.48	-0.09	1.11	33.2	11.06	24.11	45.7	0.88	1.4	3.98
	Kloostri III (Avg)	1.71	4.19	30.59	1.15	0.88	8.96	0.8	1.63	0.54	0.75	7.01	700.81	839.08	380.65	395.07	3.81	3.95	-3.26	-0.73	26.8	4.53	28.49	33.09	0.09	0.63	1.77
	Kloostri III (Min)	0.83	2.8	23.83	1.07	0.81	8.01	0.74	0.66	0.4	0.7	5.35	650.33	764.59	194.7	207.68	1.95	2.08	-6.07	-2.87	22.14	2.31	23.94	23.06	0.02	0.15	0.68
	Kloostri III (Max)	2.14	5.7	38.9	1.24	1.	9.76	0.85	5.22	0.84	0.86	7.69	725.62	894.46	740.51	756.98	7.41	7.57	-2.29	0.43	30.94	7.14	39.78	37.23	0.19	1.22	2.85
Naissaare	**Naissaare I (Avg)**	2.96	4.85	27.32	1.29	0.96	8.61	0.83	0.71	0.41	0.8	6.59	717.19	855.63	282.69	295.85	2.83	2.96	-2.55	-1.44	28.2	7.83	18.46	38.01	0.25	0.59	2.41
	Naissaare I (Min)	2.68	3.88	22.25	1.2	0.82	7.88	0.8	0.53	0.35	0.75	5.1	690.57	826.57	74.27	85.09	0.74	0.85	-3.12	-1.86	20.93	5.99	17.17	33.93	0.14	0.49	1.86
	Naissaare I (Max)	3.67	6.23	31.49	1.34	1.04	9.46	0.86	0.85	0.46	0.84	7.61	772.4	883.38	692.17	708.49	6.92	7.08	-1.78	-0.96	32.85	8.84	20.13	43.96	0.58	0.67	3.54
	Naissaare II (Avg)	2.45	7.61	19.33	1.19	0.98	9.38	0.88	0.53	0.31	0.81	8.04	710.56	809.53	392.43	407.14	3.92	4.07	-1.63	-1.54	26.37	5.91	23.3	39.11	0.25	0.51	2.22
	Naissaare II (Min)	1.96	6.34	16.72	1.18	0.97	9.01	0.86	0.2	0.17	0.81	7.68	690.65	783.13	246.97	260.66	2.47	2.61	-3.09	-2.52	23.76	5.58	20.9	35.25	0.16	0.42	1.82
	Naissaare II (Max)	2.94	8.88	21.95	1.19	0.99	9.74	0.9	0.85	0.46	0.81	8.39	730.47	835.92	537.89	553.61	5.38	5.54	-0.17	-0.56	28.99	6.24	25.7	42.96	0.35	0.61	2.62
Riga	**Riga (Avg)**	3.27	10.7	17.47	1.14	1.	8.94	0.89	5.43	0.78	0.8	8.14	713.16	829.45	201.61	214.52	2.02	2.15	-5.97	-3.43	29.81	1.32	18.36	40.07	0.49	0.85	3.41
	Riga (Min)	1.8	4.36	9.84	1.01	0.92	7.2	0.81	1.91	0.66	0.71	6.17	688.54	774.7	94.31	105.47	0.94	1.05	-8.45	-4.7	29.55	0.45	16.11	27.41	0.16	0.48	2.3
	Riga (Max)	4.15	16.34	29.04	1.38	1.15	9.83	0.94	11.16	0.92	0.87	9.13	755.9	935.77	255.51	269.3	2.56	2.69	-3.41	-2.55	30.09	2.24	21.79	46.67	1.02	1.14	4.77

Table 2. Major-element ratios include $\frac{K_2O}{Na_2O}$, $\frac{FeO^*}{MgO}$, $Mg\#_{[wt.\%]} = 100 \cdot \frac{MgO}{MgO+FeO^*}$, and $MALI_{[wt.\%]} = (Na_2O + K_2O) - CaO$. Aluminosity indices are expressed as $A/NK_{[mol]} = \frac{Al_2O_3}{Na_2O+K_2O}$ and $ASI_{[mol]} = \frac{Al_2O_3}{CaO+Na_2O+K_2O}$, with total alkalis given by $Na_2O + K_2O$. Iron enrichment is quantified using $FeO^*/(FeO^* + MgO)$. $Fe^{3+}\#_{[wt.\%]} = \frac{Fe_2O3}{FeO+Fe_2O3}$. $X_{Mag} = \frac{Mag}{(Mag+Ilm)}$. Temperature estimates are reported as T_{SiO_2} and T_{MgO}, while pressure conditions are constrained using P_{Qz} [kbar] and P_{Ab-Or} [kbar]. Analysis of major elemental relationships in the analysed rapakivi samples. Multi-dimensional discriminant functions $DF1$ and $DF2$, based on tectonic discrimination after Verma et al. (2013), are defined as: $DF1 = 0.051 \ln \frac{TiO_2}{SiO_2} + 0.226 \ln \frac{Al_2O_3}{SiO_2} - 1.77 \ln \frac{Fe_2O_3}{SiO_2} + 1.83 \ln \frac{FeO}{SiO_2} - 0.065 \ln \frac{MnO}{SiO_2} + 0.134 \ln \frac{MgO}{SiO_2} + 0.225 \ln \frac{CaO}{SiO_2} + 0.742 \ln \frac{Na_2O}{SiO_2} - 1.78 \ln \frac{K_2O}{SiO_2} + 0.146 \ln \frac{P_2O_5}{SiO_2} - 2.12$, and $DF2 = 1.09 \ln \frac{TiO_2}{SiO_2} - 1.65 \ln \frac{Al_2O_3}{SiO_2} - 1.19 \ln \frac{Fe_2O_3}{SiO_2} + 1.03 \ln \frac{FeO}{SiO_2} + 0.82 \ln \frac{MnO}{SiO_2} + 0.026 \ln \frac{MgO}{SiO_2} + 0.023 \ln \frac{CaO}{SiO_2} + 0.212 \ln \frac{Na_2O}{SiO_2} + 0.085 \ln \frac{K_2O}{SiO_2} - 0.85 \ln \frac{P_2O_5}{SiO_2} + 2.54$. Normative mineralogy is derived from $CIPW$ calculations and includes Qtz (Quartz), An (Anorthite), Ab (Albite), Or (Orthoclase), Ap (Apatite), Ilm (Ilmenite), and Mag (Magnetite).

than Phase II. Riga is distinguished by particularly low CaO, remaining close to or below 1 $wt.\%$, despite a wider MgO distribution.

The alkali distributions are dominated by K enrichment but differ in the relative abundances of Na_2O and K_2O. Wiborg contains moderate Na_2O and elevated K_2O, whereas Taebla is shifted towards more strongly potassic compositions. Ereda combines low Na_2O with high K_2O, producing one of the most pronounced K-rich distributions in the dataset. Within Neeme, Phase Ia has moderate alkali contents, Phase Ib occupies a similar but wider compositional interval, and Phase II shows no substantial increase in total alkalis despite its higher silica content. Onas is comparatively sodic and compositionally homogeneous. Within the Märjamaa-Kloostri system, K_2O increases from Märjamaa Phase I to Märjamaa Phase II, where individual values exceed 7 $wt.\%$, and then decreases in Kloostri Phase III. In contrast, Na_2O decreases slightly from Phase I to Phase II before shifting towards higher values in Phase III, locally approaching 5 $wt.\%$. This distinguishes the relatively sodic Kloostri leucogranitic phase from the more potassic Märjamaa phases. Naissaare Phase I is strongly potassic but relatively Na poor, whereas Phase II is shifted towards higher Na_2O and K_2O, although this comparison is based on only two samples. Riga occupies the most strongly K-enriched interval, with K_2O locally approaching 8 $wt.\%$, and combines this enrichment with comparatively low Na_2O and CaO.

https://doi.org/10.5194/egusphere-2026-4451
Preprint. Discussion started: 22 September 2026

P_2O_5 is generally low but is enriched and more variable in the less evolved groups. Wiborg spans values from near the detection limit to $\sim 0.5wt.\%$, whereas Taebla and Ereda occupy lower intervals. Within Neeme, Phase Ia contains moderately elevated P_2O_5, Phase Ib is slightly richer and more variable, and Phase II is distinctly depleted. Onas is uniformly poor in P_2O_5. Märjamaa Phase I shows the widest and most enriched distribution among the Estonian bodies, also reaching $\sim$ $0.5\ wt.\%$, followed by pronounced decreases in Märjamaa Phase II and Kloostri Phase III. Naissaare Phases I and II have similar central distributions, although Phase I is more variable. Riga shows moderately elevated and variable P_2O_5 contents relative to most evolved phases.

SO_3 concentrations remain low overall. Wiborg, Ereda, and Onas occupy the lowest intervals, whereas Taebla is more variable. Within Neeme, SO_3 increases slightly from Phase Ia to Phase Ib and then decreases in Phase II. Märjamaa Phase I displays the greatest sulfur variability, reaching $\sim 0.55\ wt.\%$, whereas Märjamaa Phase II and Kloostri Phase III occupy lower and more restricted intervals. Naissaare Phase I shows uniform moderate values, while Phase II extends towards lower concentrations. Riga contains relatively low and restricted SO_3 contents. Because sulfur may be hosted in accessory or secondary phases, its distribution is not interpreted as a direct indicator of differentiation.

LOI (loss on ignition) values are available only for Estonian samples and consistently remain low. Taebla and Ereda have limited distributions. In Neeme, LOI slightly decreases from Phase Ia to Phase Ib and Phase II, with overlapping distributions. In the Märjamaa-Kloostri system, LOI trends lower from Märjamaa Phase I to II and then to Kloostri Phase III. The two Naissaare phases share similar distributions, while the Riga samples have the widest range, reaching about $1.9wt.\%$. LOI indicates potential changes like secondary alteration or hydration, making it a descriptive term rather than a strict measurement.

https://doi.org/10.5194/egusphere-2026-4451
Preprint. Discussion started: 22 September 2026

(a)

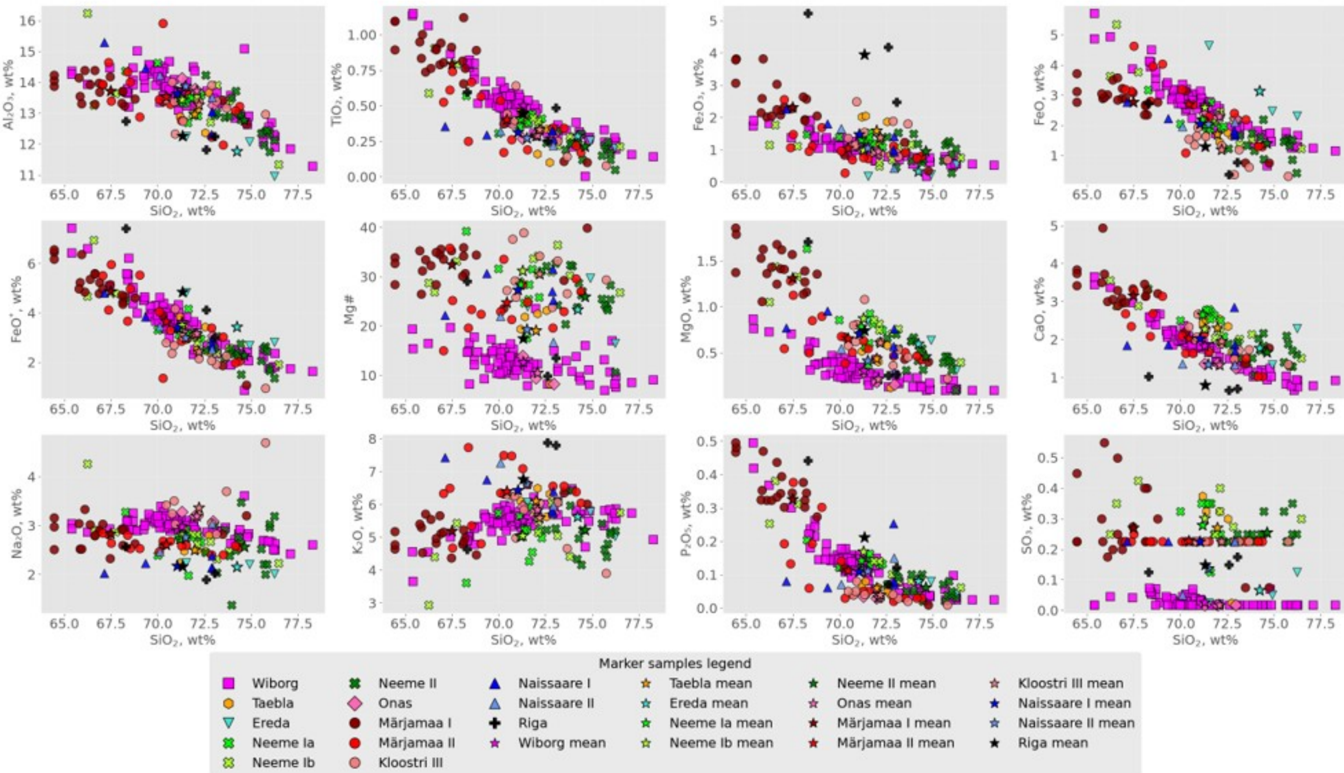

(b)

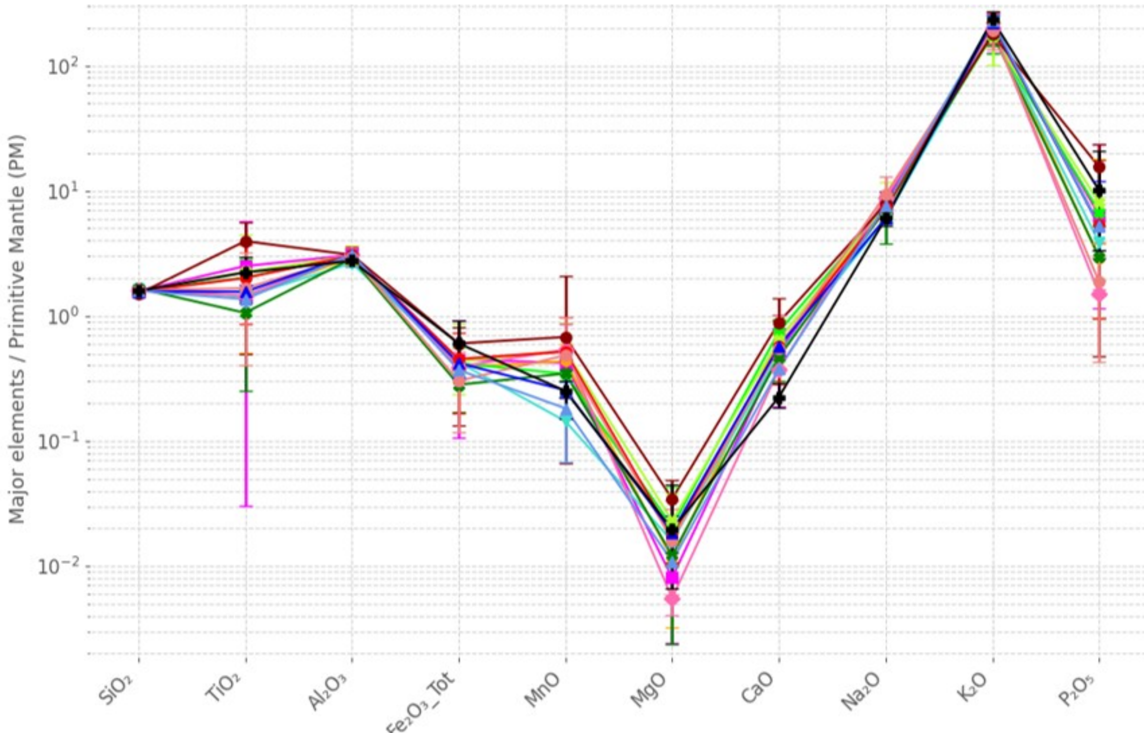

https://doi.org/10.5194/egusphere-2026-4451
Preprint. Discussion started: 22 September 2026

Figure 2. Major-element geochemical variation and normalised compositional patterns of the Estonian rapakivi intrusions and the Finnish Wiborg and Onas bodies. **(a)** Harker variation diagrams of selected major-element oxides versus SiO_2. Samples analysed in the present study are classified by intrusion and, where recognised, by magmatic phase, as shown in Figure 1c. Enlarged star symbols represent the arithmetic mean of each intrusion or phase group. Oxide concentrations are reported in $wt\%$. **(b)** Primitive Mantle (PM; Sun and McDonough (1989)) normalised major-element compositional patterns for the same rapakivi intrusions and magmatic phases.

4.2 $CIPW$ Normative trends

The distributions of the principal $CIPW$ normative components are shown in Figure 3, with summary statistics reported in Table 2.

Wiborg displays the broadest normative ranges, reinforcing its interpretation as a composite intrusion. Quartz is strongly inversely related to anorthite ($r = -0.83$), whereas magnetite, ilmenite, and apatite covary closely ($r = 0.89$-0.97), separating quartz-alkali-feldspar-rich compositions from a calcic feldspar-Fe-Ti-P association (Fig.S1). Taebla is comparatively orthoclase rich, averaging $\sim 36\%$, and contains relatively modest accessory-phase abundances. Together with locally prominent fluorite, this potassic character is consistent with late-stage differentiation and fluid involvement (Soesoo, 1993; Klein et al., 1994). Ereda combines high normative quartz, averaging $\sim 35\%$, with low albite, showing that its silica enrichment did not involve uniform enrichment of all felsic normative components. Its three-sample population, however, does not permit robust distinction between feldspar fractionation and inherited melt composition.

In Neeme, Phase Ia retains the highest mean normative anorthite of the three phases, $\sim 9.3\%$, together with moderate apatite, ilmenite, and magnetite. The inverse anorthite-orthoclase relationship strengthens from Phase Ia ($r = -0.78$) to Phase Ib ($r = -0.95$), while magnetite, ilmenite, and apatite remain strongly coupled. Phase Ib therefore preserves a similar average feldspar framework but greater internal heterogeneity, potentially reflecting variable crystal proportions or incomplete homogenisation. Phase II differs more fundamentally: normative quartz rises to $\sim 35\%$, whereas anorthite, apatite, ilmenite, and magnetite decline. The weakening of quartz-accessory-phase coupling indicates that Phase II represents a reorganised residual melt rather than a simple silica-rich continuation of the early phases. Petrographic assemblages of microcline, plagioclase, quartz, biotite, and local intergranular albite support a syenogranitic differentiation pathway (Klein et al., 1994; Rämö et al., 1996).

Onas is comparatively rich in both albite and orthoclase and displays little internal variation. Its mean normative apatite content is only $\sim 0.07\%$, consistent with strong phosphate depletion, although its three analyses cannot establish whether this restricted range characterises the entire body.

Märjamaa Phase I contains the strongest calcic feldspar-Fe-Ti-P association among the Estonian groups. Normative anorthite, apatite, ilmenite, and magnetite average $\sim 9.3\%$, 0.75%, 1.51%, and 3.25%, respectively, and the strong covariance among these components is consistent with coordinated crystallisation or accumulation of calcic plagioclase and accessory phases. Petrographic observations of comparatively calcic plagioclase and biotite-titanite-oxide clusters independently support this interpretation (Rämö et al., 1996). Märjamaa Phase II records pronounced orthoclase enrichment, averaging $\sim 37.8\%$, after substantial depletion of the earlier calcic and accessory assemblage. The inverse relationship between orthoclase and the oxide-phosphate components is consistent with development of a potassic residual melt (Rämö et al., 1996). Kloostri Phase III does not continue this orthoclase-enrichment trend. Instead, normative albite increases to $\sim 28.5\%$, while anorthite and apatite

https://doi.org/10.5194/egusphere-2026-4451
Preprint. Discussion started: 22 September 2026

decrease to $\sim 4.5\%$ and 0.09%. The decoupling of anorthite from magnetite, ilmenite, and apatite indicates a distinct late-stage feldspar regime, consistent with its leucocratic, accessory-poor, and locally fluorite-bearing character (Soesoo and Niin, 1992; Klein et al., 1994).

Naissaare Phase I is strongly potassic and comparatively albite poor, averaging $\sim 38\%$ orthoclase and 18.5% albite. Its alkali-feldspar-hornblende-biotite assemblage and comparatively calcic plagioclase are compatible with a less evolved, crystal-bearing magma (Rämö et al., 1996). Phase II shifts towards higher albite and total alkalis and lower anorthite and oxide contents, suggesting evolution towards a more alkaline and relatively sodic residual melt. This interpretation remains provisional because only two Phase II analyses are available. Riga represents the most orthoclase-rich and anorthite-poor end-member, averaging $\sim 40\%$ orthoclase and only 1.3% anorthite.

These contrasting residual compositions show that calcic feldspar and accessory-phase fractionation was regionally important, but its products were reservoir specific.

The normative correlation matrices are shown in Figure S1. Only mineralogically coherent Pearson correlations with $r < 0.05$ are highlighted; Ereda, Onas, Naissaare Phase II, and Riga are excluded because of very small sample sizes, and Taebla and Naissaare Phase I are interpreted cautiously. In Wiborg, quartz increases as anorthite decreases ($r = -0.83$), while magnetite, ilmenite, and apatite covary strongly ($r = 0.89$-0.97), separating quartz-rich from calcic feldspar-Fe-Ti-P assemblages. Taebla shows a similar quartz-orthoclase contrast ($r = -0.94$) and strong magnetite-ilmenite coupling. In Neeme, the anorthite-orthoclase opposition strengthens from Phase Ia ($r = -0.78$) to Phase Ib ($r = -0.95$), with magnetite, ilmenite, and apatite remaining tightly linked; in Phase II, magnetite and ilmenite still covary ($r = 0.93$), but quartz is no longer correlated with the oxide assemblage. Märjamaa Phase I shows the same anorthite-orthoclase opposition ($r = -0.85$) and strong Fe-Ti-P coupling ($r = 0.85$-0.92), while in Phase II the accessory-phase association persists but quartz is less involved. Kloostri Phase III is marked by inverse quartz-orthoclase ($r = -0.77$) and albite-orthoclase ($r = -0.70$) relations, with magnetite, ilmenite, and apatite still strongly coupled ($r = 0.92$-0.95).

Collectively, the better-sampled groups show persistent covariance among magnetite, ilmenite, and apatite, but the changing relationships of this assemblage with anorthite, quartz, and orthoclase record body- and phase-specific differentiation rather than a uniform regional process. Across the better-sampled groups, normative magnetite, ilmenite, and apatite consistently show strong positive covariance, indicating tightly coupled Fe-Ti oxide and phosphate components. Anorthite commonly joins this assemblage in Wiborg, Neeme Phase Ia, and Märjamaa Phases I-II, but decouples in Kloostri Phase III. Quartz generally opposes the oxide-phosphate assemblage in Wiborg, Neeme Phase Ib, and Märjamaa Phase I, but this relationship weakens or vanishes in Neeme Phase II and Märjamaa Phase II.

4.3 Statistical analysis of major-element compositions

4.3.1 Compositional data preparation

All 186 analyses contained complete, finite, and strictly positive values for the ten major-element variables used in the compositional analysis. No samples were removed and no zero replacement was required. Before closure, the selected oxide

https://doi.org/10.5194/egusphere-2026-4451
Preprint. Discussion started: 22 September 2026

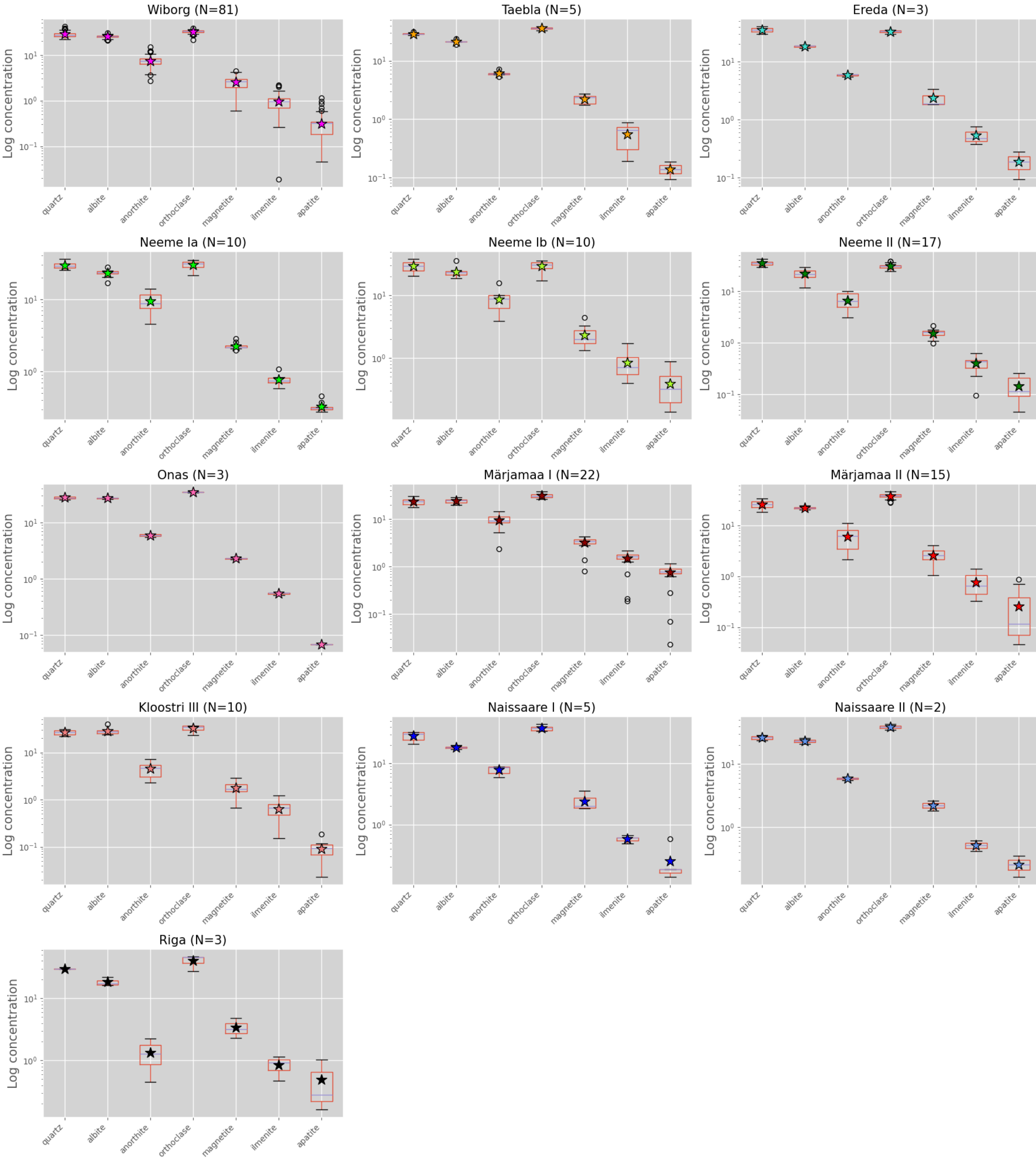

Figure 3. Boxplots displaying the $CIPW$ normative mineral components for each intrusion or respective phase of the studied rapakivi bodies.

https://doi.org/10.5194/egusphere-2026-4451
Preprint. Discussion started: 22 September 2026

sums ranged from 99.4759 to 99.9802 $wt.\%$, with a mean of 99.8705 $wt.\%$. Following closure, all compositions summed to 100 $wt.\%$ within numerical precision. The CLR matrix contained only finite values, and the maximum absolute CLR row sum was 2.887×10^{-15} (Tables S1-S2).

4.3.2 Compositional principal-component analysis

The first five components explain 97.10% of the total compositional variance (Table S3-S4). PC1 explains 53.88%, PC2 20.12%, and the first two components together 74.01% (Figs. 4a1,a2).

PC1 has its strongest positive loading in P_2O_5 (0.597), with additional positive contributions from TiO_2 (0.314) and MgO (0.299). Negative loadings are strongest for K_2O (−0.374), SiO_2 (−0.353), Na_2O (−0.316), and Al_2O_3 (−0.290). PC2 is dominated by positive MgO (0.801) and negative MnO (−0.464), with a smaller negative contribution from TiO_2 (−0.271).

Wiborg occupies the broadest sample field and has a centroid near neutral PC1 and negative PC2 values (Fig. 4a2). Taebla lies at negative PC1 and slightly positive PC2. Ereda has the highest positive PC2 centroid. Neeme Phases Ia and Ib occupy similar positive-PC1 and positive-PC2 positions, whereas Phase II shifts markedly towards negative PC1. Onas has the most negative PC1 centroid and negative PC2 values.

Märjamaa Phase I has the most positive PC1 centroid in the dataset. Märjamaa Phase II shifts towards slightly negative PC1, and Kloostri Phase III shifts farther towards negative PC1. Naissaare Phase I lies near neutral PC1 and positive PC2, whereas Phase II shifts towards negative PC1. Riga occupies positive PC1 and near-neutral PC2 values.

4.3.3 Hierarchical clustering of CLR phase centroids

Hierarchical clustering of the ten-dimensional CLR phase centroids resolves two principal branches (Fig. 4b; Tables S3-S5). The first comprises Onas, Kloostri Phase III, Märjamaa Phase II, Taebla, and Neeme Phase II. Taebla and Neeme Phase II form the closest pair in this branch, followed successively by Märjamaa Phase II and Kloostri Phase III. Onas joins at a substantially higher linkage distance.

The second branch includes Märjamaa Phase I, Naissaare Phase I, Neeme Phases Ia and Ib, Ereda, Naissaare Phase II, Wiborg, and Riga. Neeme Phases Ia and Ib form the closest pair in the complete dendrogram. Naissaare Phase I joins this subgroup, followed by Märjamaa Phase I. Ereda and Naissaare Phase II form a separate pair, while Wiborg and Riga form another subgroup at a higher linkage distance.

Because the clustering uses all ten CLR coordinates, dendrogram proximity does not necessarily reproduce proximity in the PC1-PC2 projection. The centroid positions of Ereda, Onas, Naissaare Phase II, and Riga are based on fewer than five samples.

https://doi.org/10.5194/egusphere-2026-4451
Preprint. Discussion started: 22 September 2026

(a)

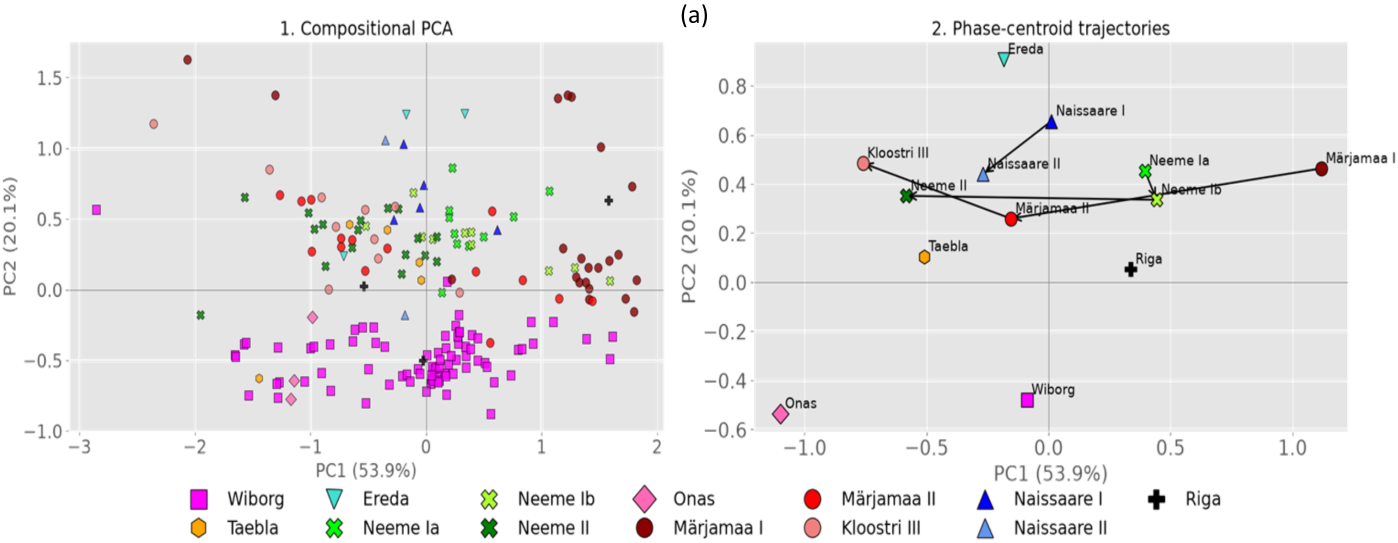

(b)

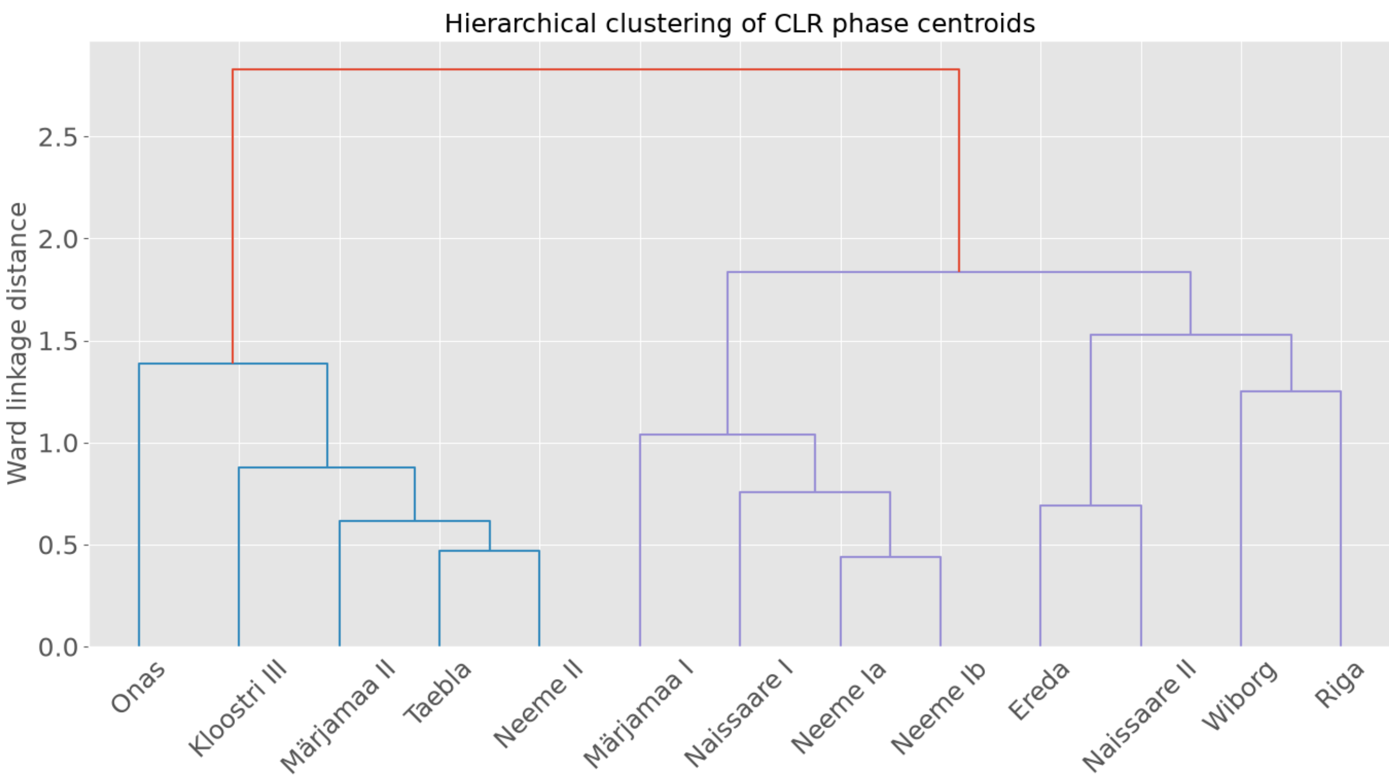

Figure 4. Compositional relationships among the analysed rapakivi **(a)** Principal-component analysis of individual samples, (1) where PC1 and PC2 explain 53.9% and 20.1% of the total compositional variance, respectively. (2) Phase-centroid positions in PCA space, with arrows illustrating the compositional trajectories of the Neeme, Märjamaa-Kloostri, and Naissaare multiphase systems. **(c)** Hierarchical clustering of phase centroids using Euclidean distances in CLR space and Ward linkage. The clustering reflects similarities in relative major-element composition and is not interpreted as direct evidence of genetic relationships among the plutons or phases.

https://doi.org/10.5194/egusphere-2026-4451
Preprint. Discussion started: 22 September 2026

4.4 Petrogenesis

Sample distributions along the $CaO/(FeO + MgO + TiO_2)$ $vs.$ Al_2O_3 trend confirm an A-type affinity (Dall'Agnol and de Oliveira, 2007) (Fig.S2a). The Al_2O_3 contents fall predominantly within the usual A-type interval of 11-14 $wt.\%$, although more aluminous compositions occur locally, as documented in other rapakivi suites (Dall'Agnol and de Oliveira, 2007; Duchesne et al., 2010; Grabarczyk et al., 2023). In the An-Ab-Or (Barker, 1979; Luo et al., 2024) and TAS diagrams (Le Maitre, 2002) (Figs.5a,b), the analysed granitoids extend from quartz monzonite-granodiorite to granite compositions, consistent with established Fennoscandian rapakivi trends (Kosunen, 1999; Rämö and Haapala, 1995; Haapala et al., 2005; Grabarczyk et al., 2023). Wiborg shows the broadest compositional range, while Taebla is more restricted and rich in orthoclase. Ereda is quartz-rich and poor in albite. Neeme Phases Ia and Ib overlap significantly, but Phase II has more quartz and less calcic feldspar. Onas is notable for its high albite and orthoclase content. Märjamaa Phase I is rich in anorthite, whereas Phase II is strong in orthoclase. Kloostri Phase III shifts towards higher albite content. Naissaare Phase I is highly potassic, and Phase II is slightly richer in orthoclase. Riga has the lowest anorthite content and high orthoclase levels. Total alkalis $(Na_2O + K_2O)$ are consistently high across all samples (Fig.5b).

The samples range from alkali-calcic to alkali compositions (with $MALI > 3.8$) and are mainly metaluminous to marginally peraluminous (with $ASI \lesssim 1.0$) (Table 2; Figs.5c, S2b). Wiborg exhibits the broadest alkalinity, including both metaluminous and weakly peraluminous compositions, while Taebla and Ereda are primarily metaluminous. In Neeme, $MALI$ increases from Phase Ia to Phase II, with ASI shifting towards the metaluminous-peraluminous boundary. Onas remains consistently alkaline near this boundary. Märjamaa Phase I is less alkaline than Phase II, and Kloostri Phase III has high $MALI$ but reverts to more metaluminous compositions. Naissaare shows an increase in alkalinity from Phase I to Phase II, both close to the boundary. Riga is the most alkaline and generally lies at this boundary, indicating that increased alkalinity does not result in a uniform increase in alumina saturation across the intrusive systems.

In the K_2O-SiO_2 diagram (Rickwood, 1989), the samples fall predominantly within the high-K alkaline series and overlap the field of Finnish rapakivi granitoids (Fig.S2c; Kosunen, 1999; Rämö and Haapala, 1995, 2005). The relative partitioning between K_2O and Na_2O varies substantially among bodies. Wiborg has a moderate K_2O/Na_2O ratio, Taebla is more potassic, and Ereda is slightly more potassic still. Neeme Phases Ia and Ib have comparable and relatively low ratios, whereas Phase II is modestly more potassic. Onas remains relatively Na-rich. Märjamaa Phase I has a moderate ratio, Phase II records pronounced K enrichment, and Kloostri Phase III shifts towards relative Na enrichment. Naissaare Phase I is among the most potassic groups, while Phase II has a lower ratio despite its higher total alkali content. Riga records the highest average K_2O/Na_2O ratio.

In the geochemical discrimination diagrams of Frost et al. (2001), the analysed samples plot predominantly within the ferroan A-type granite field (Figs.5d,e), overlapping typical Finnish rapakivi granites (Soesoo and Hade, 2012; Grabarczyk et al., 2023; Hinchey et al., 2024). Wiborg occupies the strongly ferroan part of the regional field, Taebla and Ereda are less extreme, Neeme Phases Ia and Ib are comparatively less ferroan than Phase II, and Onas is the most Fe enriched relative to Mg.

https://doi.org/10.5194/egusphere-2026-4451
Preprint. Discussion started: 22 September 2026

Märjamaa Phase I is less ferroan than Phase II, while Kloostri Phase III shifts back towards lower Fe enrichment. Naissaare Phase II is more ferroan than Phase I, and Riga also occupies the strongly ferroan range.

$FeO*/MgO$ ratios constrain melt evolution, with values < 4 indicating weak fractionation and values of 4-16 characteristic of fractionated A-type felsic granites (Whalen et al., 1987; Bonin, 2007). Wiborg has significantly elevated ratios, while Taebla and Ereda show intermediate enrichment. The Neeme sequence is non-monotonic: Phase Ia is fractionated, Phase Ib nears weak fractionation, and Phase II exhibits renewed Fe enrichment with the highest values in the pluton. Onas has the highest average ratio and is strongly fractionated. Märjamaa Phase I is near the weakly fractionated boundary, Phase II shifts towards stronger fractionation, and Kloostri Phase III returns to intermediate values. Naissaare also increases from Phase I to Phase II. Riga falls within the strongly fractionated range. These patterns indicate that iron enrichment varies across regional intrusions, and the latest phase is not always the most fractionated.

The body- and phase-dependent fractionation patterns are reflected in the $CIPW$ normative correlations (Figs.3,S1). Wiborg distinguishes between quartz-rich compositions and anorthite-magnetite-ilmenite-apatite associations. Taebla shows inverse relationships between quartz and orthoclase along with covariance in Fe-Ti oxides. Ereda's correlations are not used for body-scale processes because they are based on only three samples. In Neeme Phase Ia, anorthite correlates with oxide-phosphate components, while Phase Ib highlights stronger feldspar redistribution and coherent variations among Mag-Ilm-Ap. In Phase II, accessory components maintain positive associations, but their relationships with quartz weaken, indicating a change in differentiation. Onas correlations remain uninterpreted due to a limited sample size.

https://doi.org/10.5194/egusphere-2026-4451
Preprint. Discussion started: 22 September 2026

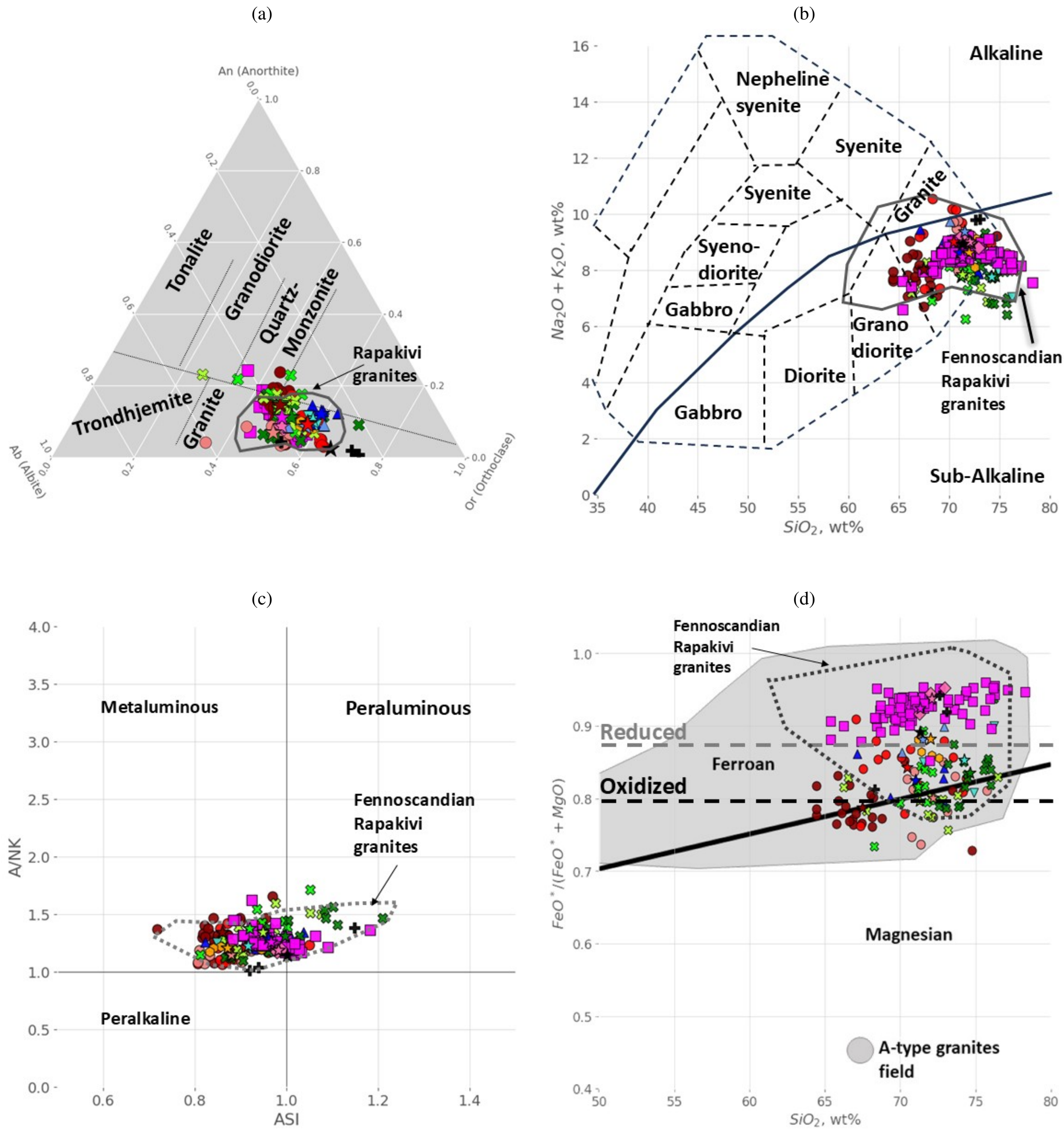

https://doi.org/10.5194/egusphere-2026-4451
Preprint. Discussion started: 22 September 2026

(e)

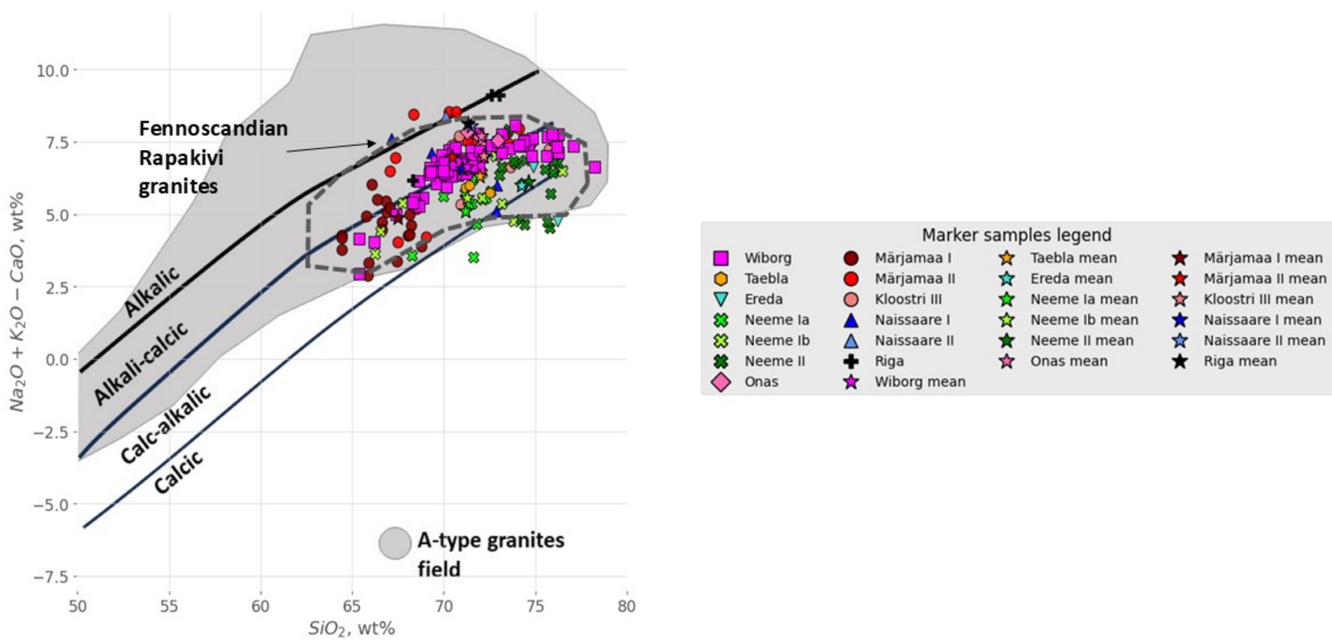

Figure 5. Geochemical classification of the analysed rapakivi granitoids. **(a)** Normative An-Ab-Or diagram of Barker (1979), with the rapakivi classification of Luo et al. (2024). **(b)** Total alkalis $(Na_2O + K_2O)$ versus SiO_2 diagram of Cox et al. (1979), following Kosunen (1999). **(c)** A/NK versus ASI diagram after Maniar and Piccoli (1989). **(d)** $FeO^*/(FeO^* + MgO)$ versus SiO_2 diagram after Frost et al. (2001), modified from Hinchey et al. (2024). **(e)** Modified alkali-lime index, $(Na_2O + K_2O - CaO)$ versus SiO_2, after Frost et al. (2001). Comparative Fennoscandian rapakivi data are based on Dall'Agnol and de Oliveira (2007); Grabarczyk et al. (2023), including data from Rämö and Haapala (1995, 2005) for the Wiborg Batholith, Kosunen (1999) for the Bodom and Obbnäs plutons, Heinonen et al. (2010b) for the Ahvenisto complex, and Sharkov (2010) for the Salmi granitoids.

Märjamaa Phase I features negative quartz-oxide relationships and positive coupling among anorthite, iron, titanium, and phosphorus (Figs.3,S1). Phase II shows a peak in orthoclase with negative orthoclase-oxide relationships. Kloostri Phase III shows a peak in albite, strong covariance among Mag-Ilm-Ap, and decouples anorthite from oxide-phosphate phases. Naissaare Phase I displays contrasting quartz-rich and orthoclase-magnetite compositions, while correlations for Naissaare Phase II and Riga are not assessed due to insufficient samples.

In the multidimensional tectonic discrimination diagram from Verma et al. (2013), defined by $DF1$ and $DF2$ (see Table 2 and Fig.6a), most samples are positioned within or near the continental-rift field, with some overlap into the collision domain, particularly from the Estonian samples. Wiborg is mainly near the rift-related area, while just a few samples from Märjamaa-Kloostri Phase II and III, Neeme Phase II and Riga match within the collision domain.

4.4.1 Redox evolution and Fe-Ti oxide systematics

A-type granites in the Laurentia-Baltica region are commonly divided into ilmenite-, magnetite-, and two-mica series (Ishihara, 1977; Anderson and Morrison, 2005; Dall'Agnol and de Oliveira, 2007). In Laurentia, magnetite-series granites typically have

https://doi.org/10.5194/egusphere-2026-4451
Preprint. Discussion started: 22 September 2026

$FeO^*/(FeO^* + MgO) = 0.80$-$0.88$, whereas ilmenite-series granites generally exceed 0.88 and are commonly interpreted as more reduced (Frost and Frost, 1997; Anderson and Morrison, 2005). Finnish rapakivi granites span a wider range of 0.79-1.00 and are generally associated with reduced A-type affinities (Rämö and Haapala, 1995, 2005; Grabarczyk et al., 2023), although their relationship to oxidised A-type granitoids remains debated (Bonin, 2007; Dall'Agnol and de Oliveira, 2007; Dall'Agnol et al., 2012). In the present dataset, Wiborg, Onas, and Riga plot predominantly within the reduced A-type fields, whereas most of the remaining Estonian samples fall within or closer to the oxidised fields in Figures 5d (Frost et al., 2001; Hinchey et al., 2024) and 6b (Dall'Agnol and de Oliveira, 2007). Within the multiphase intrusions, Neeme shifts towards more reduced ferroan compositions from Phase Ib to Phase II, Märjamaa Phase II is more reduced than Phase I before Kloostri Phase III shifts back towards lower ferroan ratios, and Naissaare Phase II includes more reduced compositions than Phase I. These diagrams therefore distinguish relative reduced and oxidised A-type affinities, but they do not independently quantify whole-rock oxidation state.

The redox interpretation of A-type granites remains controversial, particularly for oxidised, magnetite-bearing varieties sensu (Anderson and Bender, 1989; Dall'Agnol and de Oliveira, 2007). Because Fe-Mg indices incorporate both Fe^{2+} and Fe^{3+} and are strongly affected by differentiation, they primarily record bulk Fe enrichment relative to Mg. This is evident from the inverse behaviour of FeO^*/MgO and $Mg\#$. Wiborg combines a high average ratio of ~ 13 with a low average $Mg\#$ of ~ 13, whereas Onas defines the strongest ferroan end-member, with $FeO^*/MgO \sim 16$ and $Mg\# \sim 11$. Neeme shows a non-monotonic phase sequence, with $Mg\#$ increasing from Phase Ia to Phase Ib and then decreasing in Phase II. Märjamaa similarly shifts from higher $Mg\#$ in Phase I to lower values in Phase II, followed by a partial increase in Kloostri Phase III. Naissaare Phase II is more ferroan and has lower $Mg\#$ than Phase I, whereas Riga remains strongly ferroan with comparatively low $Mg\#$. These patterns are more consistent with body- and phase-specific Fe-Mg partitioning and mineral fractionation than with systematic changes in oxidation state.

Whole-rock redox state is more directly represented by the molar ferric fraction, $Fe^{3+}\# = Fe_2O_3/(FeO + Fe_2O_3)$ (Yang et al., 2021) (Table 2), although petrographic, Fe-Ti oxide, and magnetic-susceptibility data remain desirable (Dall'Agnol and de Oliveira, 2007). Lower $Fe^{3+}\#$ values indicate more reduced conditions (Ishihara, 1977, 1981, 2004); values near ~ 0.1 are very reduced, ~ 0.1-0.3 reduced, ~ 0.3-0.5 transitional, and > 0.5 oxidised (Ishihara et al., 2000; Ishihara, 2004; Yang et al., 2021). Wiborg is predominantly reduced despite its strongly ferroan character, Taebla is transitional to weakly oxidised, and Ereda is the most reduced group on average, with $Fe^{3+}\# \sim 0.11$. Neeme evolves from the transitional Phase Ia to a more reduced Phase Ib, and then to a more ferric but heterogeneous Phase II. Onas remains reduced. Märjamaa Phase I is transitional to weakly oxidised, Phase II becomes more reduced, and Kloostri Phase III becomes distinctly oxidised, with $Fe^{3+}\# \sim 0.54$. Naissaare Phase I is transitional, whereas Phase II ranges from reduced to transitional. Riga is the most oxidised end-member, with $Fe^{3+}\# \sim 0.78$, despite plotting within the reduced A-type field in the Fe-Mg discrimination diagrams. Redox evolution is therefore non-monotonic and reservoir-specific; interpretations for Ereda, Onas, Naissaare Phase II, and Riga remain provisional because each group contains fewer than 5 samples.

All bodies and phases are magnetite dominant in $CIPW$ normative terms (Fig.3), but the magnetite fraction ($X_{\mathrm{Mag}} = Mag/(Mag + Ilm)$; Solano-Acosta et al. (2026)), does not directly reproduce the $Fe^{3+}\#$ pattern. Wiborg has moderate

https://doi.org/10.5194/egusphere-2026-4451
Preprint. Discussion started: 22 September 2026

X_{Mag} despite reduced iron speciation, while Taebla and Ereda have similarly high X_{Mag} but contrasting ferric fractions. In Neeme Phase II, X_{Mag} increases even though both normative magnetite and ilmenite decrease, because ilmenite is depleted more strongly as TiO_2 declines. Onas likewise combines high X_{Mag} with reduced iron speciation. In the Märjamaa-Kloostri sequence, X_{Mag} rises from Phase I to Phase II while the absolute abundances of both oxides fall, and the oxidised Kloostri Phase III contains still lower normative oxide contents. Naissaare shows only minor change in X_{Mag} despite oxide depletion in Phase II, whereas Riga combines high ferric iron with abundant normative magnetite. Thus, $Fe^{3+}\#$ provides the more direct whole-rock redox constraint, whereas X_{Mag} and absolute magnetite-ilmenite abundances mainly reflect the combined effects of Fe-Ti availability, oxide partitioning, and magmatic differentiation.

4.4.2 Theoretical thermobarometric constraints

Whole-rock temperature (Duan et al., 2022) and pressure (Yang, 2017) proxies estimates are summarised in Table 2 and Figure 6d. Across the complete dataset, T_{SiO_2} spans approximately 610-810$°C$, whereas T_{MgO} spans approximately 700-940$°C$.

Wiborg averages approximately 713$°C$ for T_{SiO_2} and 781$°C$ for T_{MgO}. Taebla averages approximately 704$°C$ and 808$°C$, and Ereda approximately 672$°C$ and 838$°C$. Neeme Phases Ia and Ib give similar average estimates, approximately 714-715$°C$ for T_{SiO_2} and 861-871$°C$ for T_{MgO}, whereas Phase II averages approximately 666$°C$ and 816$°C$. Onas has the lowest average T_{MgO}, approximately 758$°C$.

Märjamaa Phase I gives the highest average estimates, approximately 767$°C$ and 907$°C$. These decrease to approximately 726$°C$ and 846$°C$ in Phase II and approximately 701$°C$ and 839$°C$ in Kloostri Phase III. Naissaare Phase I averages approximately 717$°C$ and 856$°C$, whereas Phase II averages approximately 711$°C$ and 810$°C$. Riga averages approximately 713$°C$ and 829$°C$.

Pressure estimates derived independently from normative quartz and from albite plus orthoclase are closely comparable (Yang, 2017). Most group averages are below 5 kbar. Wiborg averages approximately 2.5-2.6 kbar, Taebla 2.1-2.2 kbar, Ereda 1.8 kbar, Neeme 1.8-2.1 kbar, Onas 3.1-3.2 kbar, Märjamaa Phase I 4.2-4.3 kbar, Märjamaa Phase II 4.6-4.8 kbar, Kloostri Phase III 3.8-4.0 kbar, Naissaare Phase I 2.8-3.0 kbar, Naissaare Phase II approximately 4.0 kbar, and Riga 2.0-2.2 kbar.

Individual estimates exceed 7 kbar in Neeme Phase II, Märjamaa Phases I and II, Kloostri Phase III, and Naissaare Phase I. The highest values occur in Märjamaa Phase II, reaching approximately 14.3-14.5 kbar.

https://doi.org/10.5194/egusphere-2026-4451
Preprint. Discussion started: 22 September 2026

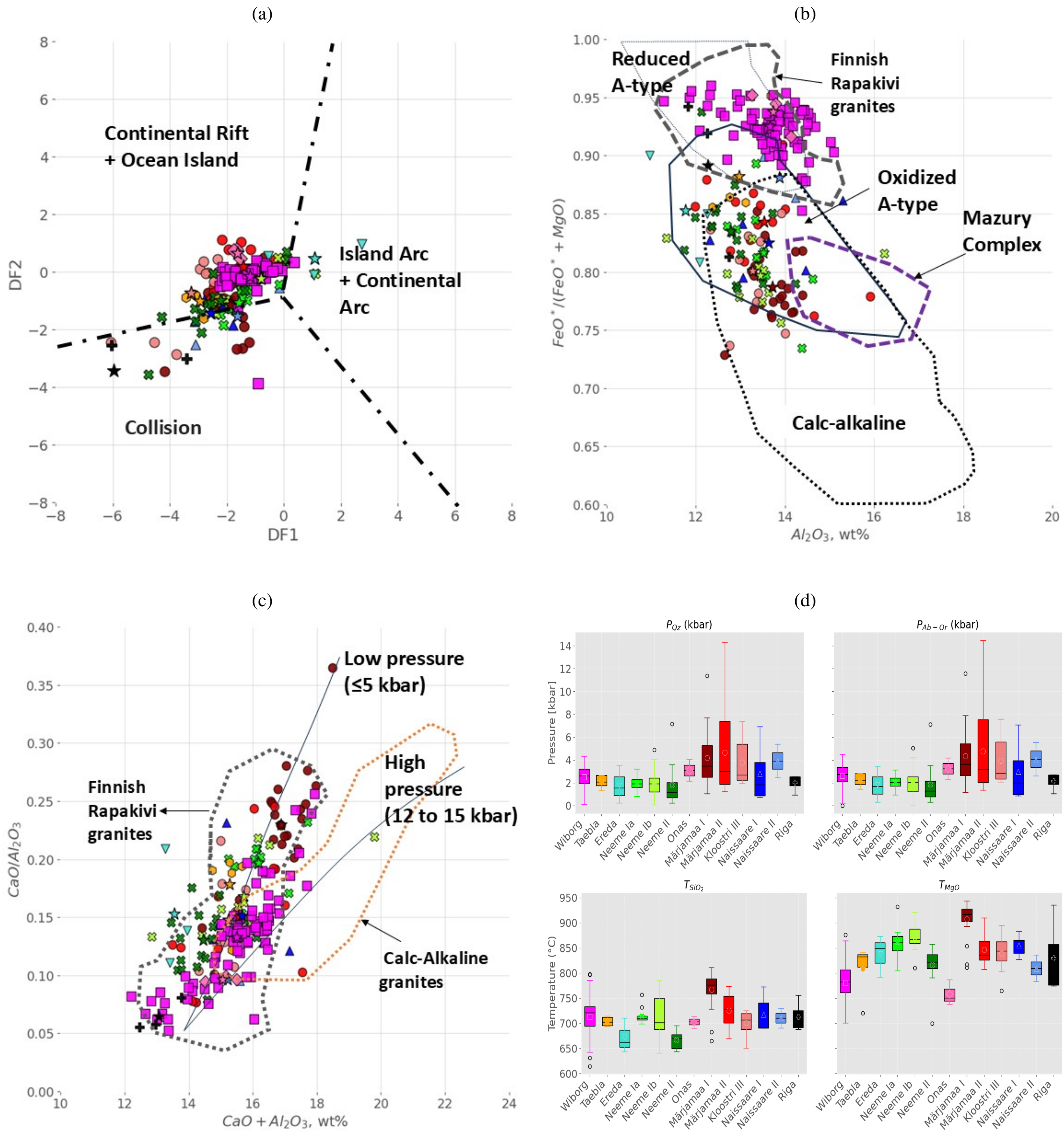

https://doi.org/10.5194/egusphere-2026-4451
Preprint. Discussion started: 22 September 2026

Figure 6. Petrogenetic classification diagrams for the analysed rapakivi granites and their respective phases. **(a)** Discriminant-function ($DF1$ and $DF2$; Table 2) multidimensional diagrams based on log-transformed major and trace element ratios for tectonic discrimination of acid granitic rocks, after Verma et al. (2013). **(b)** $FeO^*/(FeO^* + MgO)$ $vs.$ Al_2O_3 classification plot of calc-alkaline and A-type granites, including fields for reduced and oxidised subtypes, based on Dall'Agnol and de Oliveira (2007). **(c)** Whole-rock CaO/Al_2O_3 $vs.$ $CaO + Al_2O_3$ for pressure ranges in A-type granites, after Patiño Douce (1997, 1999) modified from Dall'Agnol and de Oliveira (2007). Sources of the Fennoscandian rapakivi plutons are derived from the work of Dall'Agnol and de Oliveira (2007) and references therein, while the domain corresponding to the Mazury complex domain follows Grabarczyk et al. (2023). **(d)** Thermobaormetic estimates boxplots. Legend symbols as in Figure 5.

5 Discussion

5.1 Regional compositional framework and reservoir-scale evolution

The analysed granitoids share the ferroan, high-K, alkali-calcic to alkaline characteristics typical of Fennoscandian A-type and rapakivi magmatism (Table 2; Fig.5). Nevertheless, their major-element, normative, and multivariate systematics do not define a single regional liquid line of descent. Instead, the major-element distributions and compositional statistics indicate broadly comparable differentiation processes operating within distinct magma reservoirs (Table 1; Figs.2, 4).

PC1 captures the main contrast between P_2O_5-TiO_2-MgO-rich compositions and silica-alkali-rich compositions, whereas PC2 mainly reflects relative MgO and MnO variation (Table S3; Fig. 4).

Wiborg occupies the broadest sample field and spans $\sim$ 65-78 $wt.\%$ SiO_2, consistent with its composite character and potentially with the contribution of several compositionally variable magma batches. Its centroid lies near the centre of PC1 but at negative PC2 values. Taebla is compositionally restricted and displaced towards negative PC1, consistent with its potassic and comparatively accessory-poor character.. Ereda is silica rich and has the highest positive PC2 centroid, although its position and apparent homogeneity remain provisional because only three analyses are available.

Within Neeme, Phases Ia and Ib have similar centroids and form the closest pair in the hierarchical clustering, supporting a closely related early evolution. Phase II shifts from positive to negative PC1 and occurs in the opposite principal dendrogram branch. This indicates a substantially greater compositional reorganisation between Phases Ib and II than between the two early phases. Onas has the most negative PC1 centroid and negative PC2 values, reflecting its alkali-rich, strongly Mg-depleted composition; however, its three-sample population limits body-scale interpretation.

The Märjamaa-Kloostri system defines the clearest phase trajectory. Märjamaa Phase I has the most positive PC1 centroid in the dataset, whereas Phase II and Kloostri Phase III shift successively to negative PC1 values. This displacement records decreasing relative importance of P_2O_5, TiO_2, and MgO and increasing relative importance of silica and alkalis. Their dendrogram separation further shows that some successive phases within this intrusive system are compositionally closer to phases from other bodies than to one another. Such proximity represents similarity in complete CLR major-element composition and does not imply a shared source or direct genetic relationship.

Naissaare similarly shifts towards negative PC1 from Phase I to Phase II, consistent with its more alkaline late-stage composition, although the Phase II centroid is based on only two samples. Riga occupies positive PC1 and near-zero PC2 values and

https://doi.org/10.5194/egusphere-2026-4451
Preprint. Discussion started: 22 September 2026

joins Wiborg only at a relatively high linkage distance. Their clustering therefore indicates broad multivariate similarity rather than close equivalence or a shared crystallisation history.

The PCA trajectories and hierarchical clustering therefore support phase-specific compositional evolution rather than a uniform regional differentiation trend. Neeme, Märjamaa-Kloostri, and Naissaare evolved towards distinct silica-alkali configurations, consistent with related but reservoir-specific A-type magmatism.

5.2 Feldspar and accessory-phase fractionation

The major-element and normative relationships indicate that differentiation was strongly influenced by fractionation or variable accumulation of calcic plagioclase, Mg-bearing silicates, Fe-Ti oxides, and apatite, while the residual melts became variably enriched in quartz and alkali feldspars (Tables 1 and 2; Figs.2, 3, 5a, and S1). The residual compositions nevertheless diverged towards quartz-rich, orthoclase-rich, or albite-rich end-members rather than converging on a single normative feldspar composition.

Wiborg preserves the broadest normative variability, whereas Taebla is comparatively orthoclase rich and Ereda is quartz rich but albite poor. Neeme Phases Ia and Ib retain similar feldspar and accessory-phase proportions, while Phase II is distinguished by higher quartz and lower anorthite, apatite, ilmenite, and magnetite. Onas is alkali-feldspar rich and apatite poor. The Märjamaa-Kloostri system records the clearest reorganisation, from anorthite-Fe-Ti-P enrichment in Phase I, through orthoclase enrichment in Phase II, to relative albite enrichment and accessory-phase depletion in Kloostri Phase III. Naissaare Phase II similarly shifts towards greater albite and lower anorthite and oxide contents, although it is represented by only two analyses. Riga defines the most orthoclase-rich and anorthite-poor end-member.

Overall, the normative distributions indicate differentiation from calcic feldspar- and Fe-Ti-P-bearing assemblages towards quartz- and alkali-feldspar-rich compositions, but the residual melts followed distinct pathways. Neeme Phase II evolved principally through quartz enrichment and accessory-phase depletion, Märjamaa Phase II through orthoclase enrichment, and Kloostri Phase III through relative albite enrichment. The regional bodies, therefore, do not converge towards a single normative feldspar end-member.

5.3 Ferroan differentiation and redox evolution

Major-element indices are widely used to distinguish reduced and oxidised A-type granitoids and to relate them to magma source, water content, and oxygen fugacity (Ishihara, 1977; Frost and Frost, 1997; Frost et al., 2001; Vigneresse, 2005; Bonin, 2007; Dall'Agnol and de Oliveira, 2007; Dall'Agnol et al., 2012). Reduced varieties are commonly linked to ilmenite-bearing assemblages and reduced crustal or strongly differentiated tholeiitic sources, whereas oxidised varieties may involve more hydrous and oxidised lower-crustal sources (Frost et al., 1999; Dall'Agnol et al., 1999; Anderson and Morrison, 2005; Dall'Agnol et al., 2005). However, Fe-Mg discrimination diagrams are also strongly influenced by differentiation and therefore do not independently quantify whole-rock redox state (Frost and Frost, 2011; Dall'Agnol et al., 2012).

Major-element discrimination places Wiborg, Onas, and Riga predominantly in reduced-affinity A-type fields, whereas most other Estonian samples lie within or closer to oxidised-affinity fields (Figs. 5d and 6b; Frost et al., 2001; Dall'Agnol and

https://doi.org/10.5194/egusphere-2026-4451
Preprint. Discussion started: 22 September 2026

de Oliveira, 2007; Hinchey et al., 2024). Taebla lies near the boundary, Neeme Phase II and Märjamaa Phase II shift towards more reduced-affinity compositions, and Naissaare Phase II straddles the division.

Comparison with whole-rock $Fe^{3+}\#$ shows that these ferroan fields do not consistently reflect oxidation state (Table 2). Wiborg is strongly ferroan but reduced, Taebla is transitional, and Ereda is very reduced despite plotting in the nominally oxidised-affinity fields, with average $Fe^{3+}\# \sim 0.11$. Neeme evolves non-monotonically from the transitional Phase Ia to the reduced Phase Ib, and then to a more ferric but heterogeneous Phase II. Onas combines the strongest ferroan character with reduced iron speciation. Märjamaa Phase II is more ferroan and reduced than Phase I, whereas Kloostri Phase III is less ferroan but distinctly oxidised, with $Fe^{3+}\# \sim 0.54$. Naissaare Phase II is more ferroan but less ferric than Phase I. Riga shows the clearest contradiction: it plots in the reduced-affinity fields but is the most oxidised body, with average $Fe^{3+}\# \sim 0.78$ and measured Fe_2O_3 exceeding FeO. These contrasts demonstrate that ferroan affinity and oxidation state may evolve independently within the same regional magmatic province.

All bodies and phases are magnetite dominant in $CIPW$ normative terms (Fig.3), but X_{Mag} does not reproduce the $Fe^{3+}\#$ pattern. Similar X_{Mag} values occur in Taebla and Ereda despite contrasting ferric fractions, while Neeme Phase II and Märjamaa Phase II show higher relative magnetite fractions despite depletion of both normative oxides. Kloostri Phase III is oxidised but oxide poor, whereas Riga combines high ferric iron with abundant normative magnetite. Thus, $Fe^{3+}\#$ provides the more direct whole-rock redox constraint, while ferroan indices and normative oxide proportions mainly record Fe-Mg fractionation, Fe-Ti availability, oxide partitioning, and differentiation. The regional redox diversity is therefore best explained by reservoir-specific source composition, volatile evolution, wall-rock interaction, and emplacement history rather than by a single oxidation pathway (Frost and Frost, 1997; Frost et al., 1999; Dall'Agnol and de Oliveira, 2007; Kirs et al., 2004; Salminen et al., 2021; Solano-Acosta et al., 2026). Interpretations for Ereda, Onas, Naissaare Phase II, and Riga remain provisional because of their small sample populations.

5.4 Thermal and pressure implications

The calculated temperature and pressure values are compositionally sensitive and are therefore most useful as comparative indicators rather than independent equilibrium constraints (Table 2; Figs.6c and 6d). T_{SiO_2} mainly tracks silica enrichment, whereas T_{MgO} responds to Mg-bearing phases and Fe-Ti-P fractionation (Duan et al., 2022). Similarly, the normative pressure equations depend directly on quartz, albite, and orthoclase proportions (Yang, 2017).

Most group-average normative pressures fall between ca. 2 and 5 kbar, with the highest means in Märjamaa Phase II and the lowest in Ereda and Neeme Phase II. Isolated estimates above $\sim$ 7 to 14 kbar occur in several groups but are not representative of their distributions and most likely reflect sensitivity to extreme normative quartz-feldspar proportions rather than sustained lower-crustal crystallisation (Yang, 2017; Yang et al., 2021). Most group-average normative pressures remain below $\sim 5\ kbar$ and are therefore compatible with shallow- to mid-crustal crystallisation. This range broadly agrees with published estimates of $\sim$ 2-3 $kbar$ for Salmi, 3-4 $kbar$ for Korosten, and 2.5-5.4 $kbar$ for Wiborg (Elliott, 2001; Vigneresse, 2005; Sharkov and Bogina, 2006; Sharkov, 2010; Larin, 2009). Mineral-based pressure estimates of $\sim$ 5.2-6.5 $kbar$ for Märjamaa are somewhat higher than the normative group averages (Klein et al., 1994). Mineral temperatures of $\sim$ 550-650$^{\circ}C$ probably record later

https://doi.org/10.5194/egusphere-2026-4451
Preprint. Discussion started: 22 September 2026

crystallisation or subsolidus re-equilibration rather than the melt-crystal temperatures approximated by the whole-rock formulations (Klein et al., 1994). The calculated values should therefore be used for comparative interpretation, not as substitutes for mineral-equilibrium thermobarometry.

The two temperature proxies respond to different compositional controls. T_{SiO_2} ranges from $\sim$ 610 to 810$^{\circ}C$ and averages near 710$^{\circ}C$, whereas T_{MgO} ranges from $\sim$ 700 to 940$^{\circ}C$ and averages near 820$^{\circ}C$ (Table 2; Fig.6d). The divergence between low T_{SiO_2} and higher T_{MgO} in Ereda illustrates the effects of silica enrichment and residual Mg-bearing components, whereas the low T_{MgO} of Onas reflects strong Mg depletion. The clearest phase-related decreases occur from Neeme Phases Ia-Ib to Phase II and from Märjamaa Phase I through Phase II to Kloostri Phase III. These trends are consistent with relative compositional cooling during differentiation but should not be interpreted as exact equilibrium crystallisation temperatures (Duan et al., 2022). Because T_{SiO_2} primarily tracks silica enrichment and T_{MgO} responds to Mg-bearing mineral and Fe-Ti-P fractionation, these values are best interpreted comparatively rather than as equilibrium crystallisation temperatures (Figs.3 and S1; Duan et al., 2022).

5.5 Integrated phase evolution and open-system modification

The compositional relations range from the broad composite variability of Wiborg to the internally organised phase trajectories of Neeme and Märjamaa-Kloostri (Figs.2, 3, and 4a1,a2,b). Fractional crystallisation was therefore important, but closed-system evolution alone is insufficient to explain all of the observed phase and reservoir contrasts.

Wiborg does not define a single coherent differentiation vector. Its broad major-element, normative, thermal, and pressure distributions are more consistent with a composite magma system assembled through repeated intrusive pulses. Isotopic evidence for substantial Svecofennian crustal involvement, together with mantle signatures in associated mafic rocks, supports crustal melting promoted by mantle-derived magmatism rather than direct differentiation of one parental liquid (Karell et al., 2014; Rämö et al., 2014). Taebla is more compositionally restricted, but zircon zoning, fracturing, corrosion, and late-magmatic to pneumatolytic textures indicate multistage crystallisation and late-stage modification (Klein et al., 1994). Ereda represents a quartz-rich and strongly reduced compositional end-member, although three analyses are insufficient to determine whether this reflects advanced differentiation, source composition, or limited sampling.

In Neeme, Phases Ia and Ib likely represent closely related early magma batches or connected stages within the same reservoir. Their PCA proximity and nearest-neighbour dendrogram association support this relationship. The greater dispersion of Phase Ib may reflect variable crystal proportions, local differentiation, or incomplete homogenisation rather than a fundamentally different magma source. Phase II records a more substantial transition involving quartz enrichment, removal of calcic and accessory phases, lower whole-rock temperature-proxy values, and more heterogeneous redox conditions. It is therefore best interpreted as a reorganised residual magma rather than a simple linear continuation of the Phase Ia-Ib trajectory. Onas represents a restricted, strongly Mg-depleted ferroan composition, although its three analyses do not establish body-scale homogeneity.

The Märjamaa-Kloostri system preserves the clearest evidence of multistage and potentially open-system evolution. The shift from a calcic and accessory-rich Phase I to potassic Phase II and albite-rich, oxide-poor Kloostri Phase III cannot be

https://doi.org/10.5194/egusphere-2026-4451
Preprint. Discussion started: 22 September 2026

explained by simple progressive silica enrichment and instead indicates multistage reservoir evolution Potagin (2024); Solano-Acosta et al. (2025a, 2026). This succession cannot be described solely as progressive silica enrichment because the dominant feldspar component changes from a calcic assemblage to orthoclase enrichment and finally to relative albite enrichment.

Basement xenoliths, sharp contacts, and granite apophyses in Märjamaa indicate interaction with amphibolitic to tonalitic-granodioritic gneisses (Soesoo and Niin, 1992; Klein et al., 1994). Wall-rock assimilation or episodic recharge may therefore have contributed to the elevated Ca, Mg, Ti, P, and oxide contents of Phase I. Zircon textures provide independent evidence of a multistage history: Phase I contains predominantly inclusion-rich early-magmatic grains, Phase II more strongly zoned and fractured zircon, and Kloostri Phase III cleaner late-magmatic grains, locally with inherited cores (Klein et al., 1994; Potagin, 2024). Fractional crystallisation was thus important but probably accompanied by open-system modification (Solano-Acosta et al., 2025a, 2026).

The same phase evolution has a petrophysical expression. The anorthite-, magnetite-, ilmenite-, and apatite-rich Märjamaa Phase I corresponds to comparatively high density and stronger gravity and magnetic responses. The quartz-K-feldspar-rich Phase II has lower density and magnetic susceptibility, whereas the albite-quartz-rich and oxide-poor Kloostri Phase III corresponds to the lowest densities and a marked gravity minimum (Soesoo and Niin, 1992; Soesoo, 1993; Klein et al., 1994; Solano-Acosta et al., 2025a). Local magnetic highs near Kloostri may therefore reflect underlying oxide-rich phases or feeder structures rather than the exposed leucogranite.

Naissaare records a more limited transition from a comparatively calcic, Mg-bearing, and strongly potassic Phase I to a more alkaline, albite-rich, and ferroan Phase II. Their distinct PCA centroids and dendrogram positions support a genuine phase contrast, but a complete differentiation model cannot be established from two Phase II samples. Riga represents an independent potassic and oxidised end-member rather than the terminal stage of a demonstrated regional sequence. Its association with Wiborg in the dendrogram indicates broad relative major-element similarity but does not imply a shared crystallisation history.

5.6 Geodynamic implications

Most samples plot within or near the continental-rift field, whereas only limited subsets of Neeme Phase II, Märjamaa-Kloostri Phases II-III, and Riga extend into the collision field (Table 2; Fig.6a). Because major-element discrimination functions are sensitive to differentiation, these subordinate assignments are more plausibly related to phase-specific variations in silica, alkalis, Ca, and Fe than to separate plate-tectonic regimes (Verma et al., 2003, 2013, 2022).

Wiborg is predominantly rift-related, consistent with isotopic evidence for substantial Svecofennian crustal involvement and mantle-derived contributions from associated mafic magmatism (Sharkov, 2010; Rämö et al., 2014). Taebla, Ereda, Neeme, Onas, Märjamaa-Kloostri, Naissaare, and Riga share the broader ferroan A-type affinity, but their contrasting differentiation and redox trajectories indicate reservoir- and source-specific evolution rather than derivation from a single homogeneous regional magma (Bonin, 2007; Johansson et al., 2016).

Together with geological and geophysical evidence, the regional affinity supports emplacement during post-orogenic lithospheric extension, mafic underplating, and reactivation of inherited Svecofennian structures (Soesoo and Niin, 1992; Soesoo, 1993; Korja et al., 1993; Klein et al., 1994; Kirs et al., 2004; Puura and Flodén, 2000; Rämö et al., 2000; All et al., 2006;

https://doi.org/10.5194/egusphere-2026-4451
Preprint. Discussion started: 22 September 2026

Nordbäck et al., 2024; Solano-Acosta et al., 2025a). Local transtensional to transpressional reactivation, particularly in the Märjamaa-Kloostri area, probably influenced magma ascent and emplacement geometry (Solano-Acosta et al., 2023, 2025a, 2026). High-resolution geophysical modelling remains necessary to resolve internal intrusive phases, feeder structures, and emplacement geometries in the individual bodies (Karell et al., 2009, 2014; Solano-Acosta et al., 2025a).

6 Conclusions

The analyzed rapakivi granitoids are ferroan, high-K, alkali-calcic to alkaline A-type rocks, showing distinct differentiation processes across various magma reservoirs rather than a single regional parental magma. Wiborg has the widest compositional range, while Taebla is potassic, Ereda is quartz-rich and reduced, Neeme evolves to a quartz-rich, accessory-poor Phase II, and Onas is the most ferroan and Mg-poor. Märjamaa-Kloostri exhibits clear multistage evolution, and Riga is the most potassic and ferric end-member. Differentiation mainly involved removal of calcic plagioclase and Mg-bearing minerals, leading to distinct quartz–feldspar assemblages.

A key finding is the decoupling between ferroan indices, $Mg\#$, whole-rock $Fe^{3+}\#$, and normative oxide proportions. In major-element discrimination space, Wiborg, Onas, and Riga show reduced-affinity A-type signatures, while the Estonian Wiborg-suite intrusions lie closer to oxidized-affinity fields. However, FeO^*/MgO and $Mg\#$ reflect Fe–Mg fractionation, while $Fe^{3+}\#$ captures redox evolution.

Whole-rock temperature proxies range from 610 to 810$^\circ C$ for T_{SiO_2} and 700 to 940$^\circ C$ for T_{MgO}, with average values near 710$^\circ C$ and 820$^\circ C$. Most pressure estimates are below 5 kbar, indicating shallow to mid-crustal crystallization.

Interpretations are limited by the varied analytical histories, model-dependent iron speciation for GTK samples, and unequal sample sizes. Results for Ereda, Onas, Naissaare Phase II, and Riga are provisional, suggesting that correlations should guide future research. Although CLR-PCA, hierarchical clustering, normative mineralogy, and whole-rock thermobarometric proxies can outline relative compositional evolution, they do not clarify magma sources or crystallization conditions. Future studies should prioritize additional sampling and focus on mineral chemistry, magnetite–ilmenite equilibria, redox proxies from zircon and apatite, and trace-element geochemistry.

Overall, the broader regional suite consists of related but independently evolving A-type magma reservoirs within an extensional to transtensional Fennoscandian AMCG framework. Differences in source composition, crystallization, redox conditions, volatile evolution, wall-rock interactions, and emplacement history shaped the characteristics of the individual intrusions and their phases.

Data availability. The complete compiled and processed dataset for the 186 rapakivi samples analysed in this study is provided as supplementary material.

https://doi.org/10.5194/egusphere-2026-4451
Preprint. Discussion started: 22 September 2026

Author contributions. The author conducted all aspects of the research, including conceptualization, methodology, data analysis, and writing. The author has approved the published version of the manuscript. To support language editing and clarity, the author used ChatGPT, Grammarly, and Overleaf AI-assisted tools. The author reviewed all AI-assisted text and takes full responsibility for the manuscript's accuracy and scientific content.

Competing interests. The author declares no known competing financial interests or personal ties that may have influenced the work described in this study.

Disclaimer. This research was funded and supported by the DEXPLORE Horizon Research Funds (document number VHE24051) through the Horizon Europe program HORIZON-CL4-2024-RESILIENCE-01-01. We also thank the EU Funding and Tenders Portal for its support, under project ID 101178897.

https://doi.org/10.5194/egusphere-2026-4451
Preprint. Discussion started: 22 September 2026

References

Ahl, M.: Rapakivi Granites and Related Rocks in Central Sweden: 7th International Symposium on Rapakivi Granites, July 24-26 1996, University of Helsinki, Finland: Excursion July 16-23 1996, vol. 87, Sveriges geologiska undersökning, https://resource.sgu.se/dokument/publikation/ca/ca87rapport/ca87-rapport.pdf, 1997.

Aitchison, J.: The Statistical Analysis of Compositional Data, Journal of the Royal Statistical Society: Series B, 44, 139–177, https://doi.org/10.1111/j.2517-6161.1982.tb01195.x, 1982.

Aitchison, J.: Principal Component Analysis of Compositional Data, Biometrika, 70, 57–65, https://doi.org/10.1093/biomet/70.1.57, 1983.

All, T., Puura, V., and Vaher, R.: Orogenic structures of the Precambrian basement of Estonia as revealed from the integrated modelling of the crust, in: Proceedings of the Estonian Academy of Sciences, Geology, vol. 53, pp. 165–189, Estonian Academy Publishers, https://doi.org/10.3176/geol.2004.3.03, 2004.

All, T., Flodén, T., and Puura, V.: A complex model of Mesoproterozoic sedimentary and igneous suites in a graben setting north of Gotland, Baltic Sea, GFF, 128, 53–63, https://doi.org/10.1080/11035890601281053, 2006.

Anderson, J. L. and Bender, E. E.: Nature and origin of Proterozoic A-type granitic magmatism in the southwestern United States of America, Lithos, 23, 19–52, https://doi.org/10.1016/0024-4937(89)90021-2, 1989.

Anderson, J. L. and Morrison, J.: Ilmenite, magnetite, and peraluminous Mesoproterozoic anorogenic granites of Laurentia and Baltica, Lithos, 80, 45–60, https://doi.org/10.1016/j.lithos.2004.05.008, 2005.

Andersson, U. B. and Eklund, O.: Petrology of rapakivi granites and related rocks from the Åland archipelago, SW Finland: evidence for fractional crystallization, magma mixing and late-stage enrichments, Contributions to Mineralogy and Petrology, 117, 124–136, https://doi.org/10.1007/BF00307733, 1994.

Ashwal, L. D. and Bybee, G. M.: Crustal Evolution and the Temporality of Anorthosites, Earth-Science Reviews, 173, 307–330, https://doi.org/10.1016/j.earscirev.2017.09.002, 2017.

Barker, F.: Trondhjemite: definition, environment and hypotheses of origin, in: Trondhjemites, dacites and related rocks, edited by Barker, F., vol. 6 of *Developments in Petrology*, pp. 1–12, Elsevier, Amsterdam, https://doi.org/10.1016/b978-0-444-41765-7.50006-x, 1979.

Bogdanova, S., Gorbatschev, R., Grad, M., Janik, T., Guterch, A., Kozlovskaya, E., Motuza, G., Skridlaite, G., Starostenko, V., Taran, L., et al.: EUROBRIDGE: new insight into the geodynamic evolution of the East European Craton, Geological Society, London, Memoirs, 32, 599–625, https://doi.org/10.1144/GSL.MEM.2006.032.01.36, 2006.

Bogdanova, S., Bingen, B., Gorbatschev, R., Kheraskova, T., Kozlov, V., Puchkov, V., and Volozh, Y. A.: The East European Craton (Baltica) before and during the assembly of Rodinia, Precambrian Research, 160, 23–45, https://doi.org/10.1016/j.precamres.2007.04.024, 2008.

Bogdanova, S., Gorbatschev, R., Skridlaite, G., Soesoo, A., Taran, L., and Kurlovich, D.: Trans-Baltic Palaeoproterozoic correlations towards the reconstruction of supercontinent Columbia/Nuna, Precambrian Research, 259, 5–33, https://doi.org/10.1016/j.precamres.2014.11.023, 2015.

Bonin, B.: A-type granites and related rocks: evolution of a concept, problems and prospects, Lithos, 97, 1–29, https://doi.org/10.1016/j.lithos.2006.12.007, 2007.

Branigan, N. P.: The role of shearing in the Proterozoic development of the Åland archipelago, S.W. Finland, Bulletin of the Geological Society of Finland, 59, 117–128, 1987.

Buckle, T., Williams, M., Nathwani, C. L., and Hughes, H. S.: WebNORM: a web application for calculating normative mineralogy, Frontiers in Earth Science, 11, https://doi.org/10.3389/feart.2023.1232256, 2023.

Christiansen, E. H., Haapala, I., and Hart, G. L.: Are Cenozoic topaz rhyolites the erupted equivalents of Proterozoic rapakivi granites? Examples from the western United States and Finland, Lithos, 97, 219–246, https://doi.org/10.1016/j.lithos.2007.01.010, 2007.

Cox, K. G., Bell, J. D., and Pankhurst, R. J.: The Interpretation of Igneous Rocks, Springer Book Archive, Springer Dordrecht, https://doi.org/10.1007/978-94-017-3373-1, 1979.

Dall'Agnol, R. and de Oliveira, D. C.: Oxidized, magnetite-series, rapakivi-type granites of Carajás, Brazil: Implications for classification and petrogenesis of A-type granites, Lithos, 93, 215–233, https://doi.org/10.1016/j.lithos.2006.03.065, 2007.

Dall'Agnol, R., Rämö, O. T., de Magalhães, M. S., and Macambira, M. J. B.: Petrology of the anorogenic, oxidised Jamon and Musa granites, Amazonian Craton: implications for the genesis of Proterozoic A-type granites, Lithos, 46, 431–462, https://doi.org/10.1016/S0024-4937(98)00077-2, 1999.

Dall'Agnol, R., Teixeira, N. P., Rämö, O. T., Moura, C. A. V., Macambira, M. J. B., and de Oliveira, D. C.: Petrogenesis of the Paleoproterozoic rapakivi A-type granites of the Archean Carajás metallogenic province, Brazil, Lithos, 80, 101–129, https://doi.org/10.1016/j.lithos.2004.03.058, 2005.

Dall'Agnol, R., Frost, C. D., and Ramö, O. T.: IGCP Project 510 "A-type Granites and Related Rocks through Time": Project Vita, Results, and Contribution to Granite Research, Lithos, 151, 1–16, https://doi.org/10.1016/j.lithos.2012.08.003, 2012.

Duan, M., Niu, Y., Sun, P., Chen, S., Kong, J., Li, J., Zhang, Y., Hu, Y., and Shao, F.: A simple and robust method for calculating temperatures of granitoid magmas, Mineralogy and Petrology, pp. 1–11, https://doi.org/10.1007/s00710-021-00769-5, 2022.

Duchesne, J.-C., Martin, H., Bagin´ski, B., Wiszniewska, J., and Vander Auwera, J.: The origin of ferroan-potassic A-type granitoids: the case of the hornblende–biotite granite suite of the Mesoproterozoic Mazury complex, northeastern Poland, The Canadian Mineralogist, 48, 947–968, https://doi.org/10.3749/canmin.48.4.947, 2010.

Eby, G. N.: Chemical subdivision of the A-type granitoids: petrogenetic and tectonic implications, Geology, 20, 641–644, https://doi.org/10.1130/0091-7613(1992)020<0641:CSOTAT>2.3.CO;2, 1992.

Egozcue, J. J., Gozzi, C., Buccianti, A., and Pawlowsky-Glahn, V.: Exploring geochemical data using compositional techniques: A practical guide, Journal of Geochemical Exploration, 258, 107 385, https://doi.org/10.1016/j.gexplo.2024.107385, 2024.

Eklund, O. and Shebanov, A.: The origin of rapakivi texture by sub-isothermal decompression, Precambrian Research, 95, 129–146, https://doi.org/10.1016/S0301-9268(98)00130-2, 1999a.

Eklund, O. and Shebanov, A. D.: Composition of rapakivi granite magmas: evidence from mineralogy and geochemistry in the Wiborg batholith, Finland–Russia, Contributions to Mineralogy and Petrology, 137, 181–197, https://doi.org/10.1007/s004100050591, 1999b.

Eklund, O., Fröjdö, S., and Lindberg, B.: Magma mixing, the petrogenetic link between anorthositic suites and rapakivi granites, Åland, SW Finland, Mineralogy and Petrology, 50, 3–19, https://doi.org/10.1007/BF01160135, 1994.

Elliott, B.: Crystallization conditions of the Wiborg rapakivi batholith, SE Finland: an evaluation of amphibole and biotite mineral chemistry, Mineralogy and Petrology, 72, 305–324, https://doi.org/10.1007/s007100170021, 2001.

Elo, S. and Korja, A.: Geophysical interpretation of the crustal and upper mantle structure in the Wiborg rapakivi granite area, southeastern Finland, Precambrian Research, 64, 273–288, https://doi.org/10.1016/0301-9268(93)90081-C, 1993.

Emslie, R. F.: Anorthosite Massifs, Rapakivi Granites, and Late Proterozoic Rifting of North America, Precambrian Research, 7, 61–98, https://doi.org/10.1016/0301-9268(78)90005-0, 1978.

Filzmoser, P., Hron, K., and Reimann, C.: Principal Component Analysis for Compositional Data with Outliers, Environmetrics, 20, 621–632, https://doi.org/10.1002/env.966, 2009.

https://doi.org/10.5194/egusphere-2026-4451
Preprint. Discussion started: 22 September 2026

Frost, B. R., Barnes, C. G., Collins, W. J., Arculus, R. J., Ellis, D. J., and Frost, C. D.: A geochemical classification for granitic rocks, Journal of Petrology, 42, 2033–2048, https://doi.org/10.1093/petrology/42.11.2033, 2001.

Frost, C., Frost, B., Chamberlain, K., and Edwards, B.: Petrogenesis of the 1.43 Ga Sherman batholith, SE Wyoming, USA: a reduced, rapakivi-type anorogenic granite, Journal of petrology, 40, 1771–1802, https://doi.org/10.1093/petroj/40.12.1771, 1999.

Frost, C. D. and Frost, B. R.: Reduced rapakivi-type granites: the tholeiite connection, Geology, 25, 647–650, https://doi.org/10.1130/0091-7613(1997)025<0647:RRTGTT>2.3.CO;2, 1997.

Frost, C. D. and Frost, B. R.: On ferroan (A-type) granitoids: their compositional variability and modes of origin, Journal of petrology, 52, 39–53, https://doi.org/10.1093/petrology/egq070, 2011.

Gorbatschev, R. and Bogdanova, S.: Frontiers in the Baltic shield, Precambrian Research, 64, 3–21, https://doi.org/10.1016/0301-9268(93)90066-B, 1993.

Grabarczyk, A., Wiszniewska, J., Krzemińska, E., and Petecki, Z.: A new A-type granitoid occurrence in southernmost Fennoscandia: geochemistry, age and origin of rapakivi-type quartz monzonite from the Pietkowo IG1 borehole, NE Poland, Mineralogy and Petrology, 117, 1–25, https://doi.org/10.1007/s00710-022-00799-7, 2023.

Grocott, J., Garde, A. A., Chadwick, B., Cruden, A. R., and Swager, C.: Emplacement of rapakivi granite and syenite by floor depression and roof uplift in the Palaeoproterozoic Ketilidian orogen, South Greenland, Journal of the Geological Society, 156, 15–24, https://doi.org/10.1144/gsjgs.156.1.0015, 1999.

Haapala, I.: Metallogenese der Rapakivi-Granite, Mineralogy and Petrology, 54, 149–160, https://doi.org/10.1007/BF01162858, 1995.

Haapala, I. and Rämö, O. T.: Tectonic setting and origin of the Proterozoic rapakivi granites of southeastern Fennoscandia, Earth and environmental science transactions of the Royal Society of Edinburgh, 83, 165–171, https://doi.org/10.1017/S0263593300007859, 1992.

Haapala, I., Rämö, O. T., and Frindt, S.: Comparison of Proterozoic and Phanerozoic rift-related basaltic-granitic magmatism, Lithos, 80, 1–32, https://doi.org/10.1016/j.lithos.2004.04.057, 2005.

Heinonen, A., Andersen, T., and Rämö, O.: Re-evaluation of rapakivi petrogenesis: Source constraints from the Hf isotope composition of zircon in the rapakivi granites and associated mafic rocks of southern Finland, Journal of Petrology, 51, 1687–1709, https://doi.org/10.1093/petrology/egq035, 2010a.

Heinonen, A. P., Rämö, O. T., Mänttäri, I., Johanson, B., and Alviola, R.: Formation and fractionation of high-Al tholeiitic magmas in the Ahvenisto rapakivi granite–massif-type anorthosite complex, southeastern Finland, The Canadian Mineralogist, 48, 969–990, https://doi.org/10.3749/canmin.48.4.969, 2010b.

Heinonen, A. P., Rämö, O. T., Mänttäri, I., Andersen, T., and Larjamo, K.: Zircon as a proxy for the magmatic evolution of Proterozoic ferroan granites; the Wiborg rapakivi granite batholith, SE Finland, Journal of Petrology, 58, 2493–2517, https://doi.org/10.1093/petrology/egy014, 2017.

Hinchey, A. M., Sandeman, H. A., and Butler, J. P.: The Paleoproterozoic granite factory: Voluminous post-collisional, ferroan, A-type granites and implications for crust formation and metallogenic tenor, Labrador, Canada, GSA Bulletin, 136, 893–916, https://doi.org/10.1130/B36727.1, 2024.

Hoffman, P. F.: Speculations on Laurentia's First Gigayear (2.0 to 1.0 Ga), Geology, 17, 135–138, https://doi.org/10.1130/0091-7613, 1989.

Högdahl, K., Sjöström, H., and Bergman, S.: Ductile Shear Zones Related to Crustal Shortening and Domain Boundary Evolution in the Central Fennoscandian Shield, Tectonics, 28, https://doi.org/10.1029/2008TC002277, 2009.

Ishihara, S.: The magnetite-series and ilmenite-series granitic rocks, Mining Geology, 27, 293–305, 1977.

https://doi.org/10.5194/egusphere-2026-4451
Preprint. Discussion started: 22 September 2026

Ishihara, S.: The Granitoid Series and Mineralization, in: Economic Geology Seventy-Fifth Anniversary Volume, edited by Skinner, B. J., Economic Geology Publishing Company, ISBN 9781934969533, https://doi.org/10.5382/AV75.14, 1981.

Ishihara, S.: The redox state of granitoids relative to tectonic setting and earth history: The magnetite–ilmenite series 30 years later, in: The Fifth Hutton Symposium on the Origin of Granites and Related Rocks, edited by Ishihara, S., Stephens, W. E., Harley, S. L., Arima, M., and Nakajima, T., vol. 389 of *Special Paper*, Geological Society of America, ISBN 9780813723891, https://doi.org/10.1130/0-8137-2389-2.23, 2004.

Ishihara, S., HAsHIMoTo, M., and Machida, M.: Magnetite/ilmenite–series classification and magnetic susceptibility of the Mesozoic-Cenozoic batholiths in Peru, Resource Geology, 50, 123–129, https://doi.org/10.1111/j.1751-3928.2000.tb00062.x, 2000.

Johansson, Å., Waight, T., Andersen, T., and Simonsen, S. L.: Geochemistry and petrogenesis of Mesoproterozoic A-type granitoids from the Danish island of Bornholm, southern Fennoscandia, Lithos, 244, 94–108, https://doi.org/10.1016/j.lithos.2015.11.031, 2016.

Johansson, Å., Bingen, B., Huhma, H., Waight, T., Vestergaard, R., Soesoo, A., Skridlaite, G., Krzeminska, E., Shumlyanskyy, L., Holland, M. E., Holm-Denoma, C., Teixeira, W., Faleiros, F. M., Ribeiro, B. V., Jacobs, J., Wang, C., Thomas, R. J., Macey, P. H., Kirkland, C. L., Hartnady, M. I. H., Eglington, B. M., Puetz, S. J., and Condie, K. C.: A Geochronological Review of Magmatism Along the External Margin of Columbia and in the Grenville-Age Orogens Forming the Core of Rodinia, Precambrian Research, 371, 106 463, https://doi.org/10.1016/j.precamres.2021.106463, 2022.

Johansson, : A Tentative Model for the Origin of A-Type Granitoids, Minerals, 13, 236, https://doi.org/10.3390/min13020236, 2023.

Karell, F., Ehlers, C., Airo, M.-L., and Selonen, O.: Intrusion mechanisms and magnetic fabrics of the Vehmaa rapakivi granite batholith in SW Finland, Geotectonic Research, 96, 53–68, https://doi.org/10.1127/1864-5658/09/96-0053, 2009.

Karell, F., Ehlers, C., and Airo, M.-L.: Emplacement and magnetic fabrics of rapakivi granite intrusions within Wiborg and Åland rapakivi granite batholiths in Finland, Tectonophysics, 614, 31–43, https://doi.org/10.1016/j.tecto.2013.12.006, 2014.

Kelsey, C.: Calculation of the CIPW norm, Mineralogical magazine and journal of the Mineralogical Society, 34, 276–282, https://doi.org/10.1180/minmag.1965.034.268.23, 1965.

Kirs, J., Haapala, I., and Rämö, O. T.: Anorogenic magmatic rocks in the Estonian crystalline basement, in: Proceedings of the Estonian Academy of Sciences. Geology, vol. 53, pp. 210–225, https://doi.org/10.3176/geol.2004.3.05, 2004.

Kirs, J., Puura, V., Soesoo, A., Klein, V., Konsa, M., Koppelmaa, H., Niin, M., and Urtson, K.: The crystalline basement of Estonia: rock complexes of the Palaeoproterozoic Orosirian and Statherian and Mesoproterozoic Calymmian periods, and regional correlations., Estonian Journal of Earth Sciences, 58, https://doi.org/10.3176/earth.2009.4.01, 2009.

Kivisilla, J., Niin, M., and Koppelmaa, H.: Catalogue of chemical analyses of major elements in the rocks of the crystalline basement of Estonia, Geological Survey of Estonia, Tallinn, https://kirjandus.geoloogia.info/reference/21247, 1999.

Klein, V., Konsa, M., and Niin, M.: On mineralogy of the porphyrous potassium granites of small massifs in the northern Estonian basement, Proceedings of the Estonian Academy of Sciences, Geology, 43, 165–176, https://doi.org/10.3176/geol.1994.4.01, 1994.

Korhonen, J. V., Aaro, S. F., All, T., Nevanlinna, H., Skilbrei, J. R., Säävuori, H., Vaher, R., Zhdanova, L., and Koistinen, T.: Magnetic Anomaly Map of the Fennoscandian Shield 1:2,000,000, 2002.

Korja, A. and Kosonen, E., eds.: Seismotectonic Framework and Seismic Source Area Models in Fennoscandia, Northern Europe, Report S-63, Institute of Seismology, University of Helsinki, Helsinki, Finland, 2015.

Korja, A., Korja, T., Luosto, U., and Heikkinen, P.: Seismic and geoelectric evidence for collisional and extensional events in the Fennoscandian Shield implications for Precambrian crustal evolution, Tectonophysics, 219, 129–152, https://doi.org/10.1016/0040-1951(93)90292-R, 1993.

https://doi.org/10.5194/egusphere-2026-4451
Preprint. Discussion started: 22 September 2026

Korja, A., Heikkinen, P., and Aaro, S.: Crustal structure of the northern Baltic Sea palaeorift, Tectonophysics, 331, 341–358, https://doi.org/10.1016/S0040-1951(00)00290-0, 2001.

Korsman, K., Korja, T., Pajunen, M., Virransalo, P., Group, G. W., et al.: The GGT/SVEKA transect: structure and evolution of the continental crust in the Paleoproterozoic Svecofennian orogen in Finland, International Geology Review, 41, 287–333, https://doi.org/10.1080/00206819909465144, 1999.

Kosunen, P.: The rapakivi granite plutons of Bodom and Obbnäs, southern Finland: petrography and geochemistry, Bulletin of the Geological Society of Finland, 71, 275–304, https://doi.org/10.17741/bgsf/71.2.005, 1999.

Kukkonen, I. and Lauri, L. S.: Modelling the Thermal Evolution of a Collisional Precambrian Orogen: High Heat Production Migmatitic Granites of Southern Finland, Precambrian Research, 168, 233–246, https://doi.org/10.1016/j.precamres.2008.10.004, 2009.

Lahtinen, R., Korja, A., and Nironen, M.: Paleoproterozoic tectonic evolution, in: Developments in Precambrian Geology, vol. 14, pp. 481–531, Elsevier, https://doi.org/10.1016/S0166-2635(05)80012-X, 2005.

Laitakari, I., Rämö, T., Suominen, V., Niin, M., Stepanov, K., and Amantov, A.: Subjotnian: Rapakivi granites and related rocks in the surroundings of the Gulf of Finland, Special Paper GTK, pp. 59–98, 1996.

Laitala, M.: Pellingin ja Porvoon kartta-alueiden kallioperä. Summary: Pre-Quaternary Rocks of the Pellinki and Porvoo Map-Sheet Areas, no. Sheets 3012 and 3021 in Geological Map of Finland 1:100 000, Explanation to the Maps of Pre-Quaternary Rocks, Geological Survey of Finland, 1984.

Larin, A. M.: Rapakivi Granites in the Geological History of the Earth. Part 1: Magmatic Associations with Rapakivi Granites: Age, Geochemistry, and Tectonic Setting, Stratigraphy and Geological Correlation, 17, 235–258, https://doi.org/10.1134/S0869593809030010, 2009.

Le Maitre, R.: Some Problems of the Projection of Chemical Data into Mineralogical Classifications, Contributions to Mineralogy and Petrology, 56, 181–189, 10.1007/BF00399603, 1976.

Le Maitre, R. W.: Igneous Rocks: A Classification and Glossary of Terms, Cambridge University Press, Cambridge, 2nd edn., 2002.

Loiselle, M. and Wones, D.: Characteristics and origin of anorogenic granites, Geological Society of America Abstracts with Programs, 11, 468, 1979.

Luo, F., Gong, H., and Liu, H.: Early-paleozoic rapakivi-textured granite from the North Qinling (Central China): implications for crust-mantle interactions in a post-collisional setting, Mineralogy and Petrology, pp. 1–23, https://doi.org/10.1007/s00710-024-00861-6, 2024.

Maniar, P. D. and Piccoli, P. M.: Tectonic discrimination of granitoids, Geological Society of America Bulletin, 101, 635–643, https://doi.org/10.1130/00167606(1989)101<0635:TDOG>2.3.CO;2, 1989.

Mitchell, R. N., Zhang, N., Salminen, J., Liu, Y., Spencer, C. J., Steinberger, B., Murphy, J. B., and Li, Z.-X.: The supercontinent cycle, Nature Reviews Earth & Environment, 2, 358–374, https://doi.org/10.1038/s43017-021-00160-0, 2021.

Murtagh, F. and Legendre, P.: Ward's Hierarchical Agglomerative Clustering Method: Which Algorithms Implement Ward's Criterion?, Journal of Classification, 31, 274–295, https://doi.org/10.1007/s00357-014-9161-z, 2014.

Nironen, M.: The Svecofennian Orogen: A Tectonic Model, Precambrian Research, 86, 21–44, https://doi.org/10.1016/S0301-9268(97)00039-9, 1997.

Nironen, M.: Guide to Geological Map of Finland - Bedrock 1:1,000,000, in: Bedrock of Finland at the Scale 1:1,000,000 - Major Stratigraphic Units, Metamorphism and Tectonic Evolution, edited by Nironen, M., pp. 41–76, 2017.

Nironen, M., Elliott, B., and Rämö, O. T.: 1.88-1.87 Ga post-kinematic intrusions of the Central Finland Granitoid Complex: a shift from C-type to A-type magmatism during lithospheric convergence, Lithos, 53, 37–58, https://doi.org/10.1016/S0024-4937(00)00007-4, 2000.

Nordbäck, N., Skyttä, P., Engström, J., Ovaskainen, N., Mattila, J., and Aaltonen, I.: Mesoproterozoic Strike-Slip Faulting within the Åland Rapakivi Batholith, Southwestern Finland, Tektonika, 2, 1–26, https://doi.org/10.55575/tektonika2024.2.1.51, 2024.

Patiño Douce, A. E.: Generation of metaluminous A-type granites by low-pressure melting of calc-alkaline granitoids, Geology, 25, 743–746, https://doi.org/10.1130/0091-7613(1997)025<0743:GOMATG>2.3.CO;2, 1997.

Patiño Douce, A. E.: What do experiments tell us about the relative contributions of crust and mantle to the origin of granitic magmas?, Geological Society, London, Special Publications, 168, 55–75, https://doi.org/10.1144/GSL.SP.1999.168.01.05, 1999.

Petersell, V. and Levchenkov, O.: On the geological structure of the crystalline basement of the southern slope of the Baltic Shield, Acta et Commentationes Universitatis Tartuensis, 972, 16–39, https://files.geocollections.info/bd4c7235-8435-49b4-8cbd-cd02e063ea92.pdf, 1994.

Pirajno, F. and Santosh, M.: Mantle plumes, supercontinents, intracontinental rifting and mineral systems, Precambrian Research, 259, 114–142, https://doi.org/10.1016/j.precamres.2014.12.016, 2015.

Potagin, C.: Geology, Geochemistry, and Geochronology of the Märjamaa Rapakivi Granitoid Intrusion, Master's thesis, Tallinn University of Technology, Tallinn, Estonia, https://digikogu.taltech.ee/et/Download/9ee436a4-89a6-487b-8d09-c957cb76666e, master's thesis, Department of Geology, Institute of Geology. Supervisors: Alvar Soesoo and Juan David Solano-Acosta, 2024.

Puura, V. and Flodén, T.: Subjotnian igneous structures in the Svecofennian domain of the Baltic region, GFF, 118, 22–23, https://doi.org/10.1080/11035899609546289, 1996.

Puura, V. and Flodén, T.: Rapakivi-granite–anorthosite magmatism — a way of thinning and stabilisation of the Svecofennian crust, Baltic Sea Basin, Tectonophysics, 305, 75–92, https://doi.org/10.1016/S0040-1951(99)00019-0, 1999.

Puura, V. and Flodén, T.: Rapakivi-related basement structures in the Baltic Sea area; a regional approach, GFF, 122, 257–272, https://doi.org/10.1080/11035890001223257, 2000.

Puura, V., Hints, R., Huhmah, H., Klein, V., Konsad, M., Kuldkeppa, R., Manttarih, I., and Soesoo, A.: Svecofennian metamorphic zones in the basement of Estonia, in: Proceedings of the Estonian Academy of Sciences, Geology, vol. 53, pp. 190–209, Estonian Academy Publishers, https://doi.org/10.3176/geol.2004.3.04, 2004.

Rajesh, H. M.: Characterization and origin of a compositionally zoned aluminous A-type granite from South India, Geological Magazine, 137, 291–318, https://doi.org/10.1017/S001675680000399X, 2000.

Rämö, O. T., Turkki, V., Mänttäri, I., Heinonen, A., Larjamo, K., and Lahaye, Y.: Age and isotopic fingerprints of some plutonic rocks in the Wiborg rapakivi granite batholith with special reference to the dark wiborgite of the Ristisaari Island., Bulletin of the Geological Society of Finland, 86, https://doi.org/10.17741/bgsf/86.2.002, 2014.

Rasilainen, K., Lahtinen, R., and Bornhorst, T. J.: The Rock Geochemical Database of Finland: Manual, Geological Survey of Finland, 2007.

Raukas, A. and Teedumäe, A., eds.: Geology and Mineral Resources of Estonia, Estonian Academy Publishers, Tallinn, Estonia, https://geoloogia.info/geology/index.html, ISBN 9985-50-185-3, 1997.

Rickwood, P. C.: Boundary lines within petrologic diagrams which use oxides of major and minor elements, lithos, 22, 247–263, https://doi.org/10.1016/0024-4937(89)90028-5, 1989.

Rämö, O. T. and Haapala, I.: One hundred years of rapakivi granite, Mineralogy and Petrology, 52, 129–185, https://doi.org/10.1007/BF01163243, 1995.

Rämö, O. T. and Haapala, I.: Rapakivi granites, Developments in Precambrian Geology, 14, 533–562, https://doi.org/10.1016/S0166-2635(05)80013-1, 2005.

Rämö, O. T., Huhma, H., and Kirs, J.: Radiogenic isotopes of the Estonian and Latvian rapakivi granite suites: new data from the concealed Precambrian of the East European Craton, Precambrian Research, 79, 209–226, https://doi.org/10.1016/S0301-9268(95)00083-6, 1996.

Rämö, T., Korja, A., and Haapala, I.: Evolution of the Fennoscandian lithosphere in the mid-Proterozoic: the rapakivi magmatism, in: Lithosphere 2000, edited by Pesonen, L., Korja, A., and Hjelt, S.-E., pp. 129–136, a Symposium on the Structure, Composition and Evolution of the Lithosphere in Finland ; Conference date: 04-10-2000 Through 05-10-2000, 2000.

Salminen, J., Elming, S.-Å., Mertanen, S., Wang, C., Almqvist, B., and Moakhar, M. O.: Paleomagnetic studies of rapakivi complexes in the Fennoscandian shield–Implications to the origin of Proterozoic massif-type anorthosite magmatism, Precambrian Research, 365, https://doi.org/10.1016/j.precamres.2021.106406, 2021.

Sharkov, E.: Middle-proterozoic anorthosite–rapakivi granite complexes: An example of within-plate magmatism in abnormally thick crust: Evidence from the East European Craton, Precambrian Research, 183, 689–700, https://doi.org/10.1016/j.precamres.2010.08.008, 2010.

Sharkov, E. and Bogina, M.: Evolution of Paleoproterozoic magmatism: geology, geochemistry, and isotopic constraints, Stratigraphy and Geological Correlation, 14, 345–367, https://doi.org/10.1134/S0869593806040010, 2006.

Skridlaitė, G., Whitehouse, M., and Rimša, A.: Evidence for a pulse of 1.45 Ga anorthosite–mangerite–charnockite–granite (AMCG) plutonism in Lithuania: implications for the Mesoproterozoic evolution of the East European Craton, Terra Nova, 19, 294–301, https://doi.org/10.1111/j.1365-3121.2007.00748.x, 2007.

Soesoo, A.: Estonian porphyraceous potassium granites: petrochemical subdivision and petrogenetical interpretation, in: Proceedings of the Estonian Academy of Sciences, Geology, vol. 42, pp. 97–109, https://doi.org/10.3176/geol.1993.3.01, 1993.

Soesoo, A. and Hade, S.: Geochemistry and age of some A-type granitoid rocks of Estonia, in: Seventh symposium on the structure, composition and evolution of the lithosphere in Finland, p. 97, 2012.

Soesoo, A. and Niin, M.: Petrographical and petrochemical features of the Estonian Precambrian porphyraceous potassium granites, in: Proceedings of the Estonian Academy of Science, Geology, vol. 41, pp. 93–107, https://doi.org/10.3176/geol.1992.3.01, 1992.

Soesoo, A., Puura, V., Kirs, J., Petersell, V., Niin, M., and All, T.: Outlines of the Precambrian basement of Estonia, in: Proceedings of the Estonian Academy of Sciences, Geology, vol. 53, pp. 149–164, https://doi.org/10.3176/geol.2004.3.02, 2004.

Soesoo, A., Košler, J., and Kuldkepp, R.: Age and geochemical constraints for partial melting of granulites in Estonia, Mineralogy and Petrology, 86, 277–300, https://doi.org/10.1007/s00710-005-0110-8, 2006.

Soesoo, A., Nirgi, S., and Plado, J.: The evolution of the Estonian Precambrian basement: geological, geophysical and geochronological constraints, Proceedings of the Karelian Research Centre of the Russian Academy of Sciences, pp. 18–33, https://doi.org/10.17076/geo1185, 2020.

Solano-Acosta, J. D.: Crustal Structure, Tectonics, and Magmatic Evolution of the Estonian Proterozoic Basement: Geophysical and Geochemical Insights, Ph.D. thesis, Tallinn University of Technology, Tallinn, Estonia, https://doi.org/10.23658/taltech.9/2026, 2026.

Solano-Acosta, J. D., Soesoo, A., and Hints, R.: New insights of the crustal structure across Estonia using satellite potential fields derived from WGM-2012 gravity data and EMAG2v3 magnetic data, Tectonophysics, 846, 229 656, https://doi.org/10.1016/j.tecto.2022.229656, 2023.

Solano-Acosta, J. D., Soesoo, A., and Hints, R.: Integrated geophysical and emplacement modelling of the Märjamaa and Kloostri rapakivi granitoids, Estonia: Insights into intrusion geometry and tectonic controls, Precambrian Research, 430, 107 938, https://doi.org/10.1016/j.precamres.2025.107938, 2025a.

Solano-Acosta, J. D., Soesoo, A., and Hints, R.: Geochemistry, provenance, and tectonic setting of Paleoproterozoic metasedimentary and metavolcanic units of the Estonian Alutaguse region, eastern Fennoscandia, Estonian Journal of Earth Sciences, 74, 61–82, https://doi.org/10.3176/earth.2025.05, 2025b.

Solano-Acosta, J. D., Soesoo, A., and Hints, R.: An Updated Review of Major-Element Geochemistry, Redox Systematics, and Petrogenesis of the Märjamaa and Kloostri Rapakivi Granites, Estonia, Estonian Journal of Earth Sciences, https://doi.org/10.3176/earth.2026.06, 2026.

Soosalu, H., Uski, M., Komminaho, K., and Veski, A.: Recent Intraplate Seismicity in Estonia, East European Platform, Seismological Research Letters, 93, 1800–1811, https://doi.org/10.1785/0220210277, 2022.

Sun, S.-S. and McDonough, W. F.: Chemical and isotopic systematics of oceanic basalts: implications for mantle composition and processes, Geological Society, London, Special Publications, 42, 313–345, https://doi.org/10.1144/GSL.SP.1989.042.01.19, 1989.

Suominen, V.: The chronostratigraphy of southwestern Finland with special reference to Postjotnian and Subjotnian diabases, Bulletin-Geological Survey of Finland, 1991.

Templ, M. and Hofer, C.: Compositional analysis of the relationships between the organic matter content and chemical and physical properties of soil, Applied Geochemistry, 193, 106 526, https://doi.org/10.1016/j.apgeochem.2025.106526, 2025.

Terentiev, R. A. and Santosh, M.: Baltica (East European Craton) and Atlantica (Amazonian and West African Cratons) in the Proterozoic: The Pre-Columbia Connection, Earth-Science Reviews, 210, 103 378, https://doi.org/10.1016/j.earscirev.2020.103378, 2020.

Tornroos, R.: Petrography, mineral chemistry and petrochemistry of granite porphyry dykes from Sibbo, southern Finland, Bulletin-Geological survey of Finland, 1984.

Trubitsyn, V. P., Mooney, W. D., and Abbott, D. H.: Cold cratonic roots and thermal blankets: how continents affect mantle convection, International Geology Review, 45, 479–496, 2003.

Vaasjoki, M., Rämö, O. T., and Sakko, M.: New U-Pb ages from the Wiborg rapakivi area: constraints on the temporal evolution of the rapakivi granite-anorthosite-diabase dyke association of southeastern Finland, Precambrian Research, 51, 227–243, https://doi.org/10.1016/0301-9268(91)90102-G, 1991.

Valkama, M., Sundblad, K., Nygård, R., and Cook, N.: Mineralogy and geochemistry of indium-bearing polymetallic veins in the Sarvlaxviken area, Lovisa, Finland, Ore Geology Reviews, 75, 206–219, https://doi.org/10.1016/j.oregeorev.2015.12.001, 2016.

Verma, S., Torres-Alvarado, I., and Velasco-Tapia, F.: A Revised CIPW Norm, Schweizerische Mineralogische und Petrographische Mitteilungen, 83, 197–216, https://doi.org/10.5169/seals-63145, 2003.

Verma, S. K., Torres-Sánchez, D., de León Hernández, D. A., Oliveira, E. P., Hernández-Martínez, K. R., Torres-Sánchez, S. A., Hernández, J. R. T., Moreno, J. A., Shukla, M., and Malviya, V. P.: Petrogenesis and geodynamic implications of Oligocene A-type granite in the Guadalcazar area, San Luis Potosi, central Mexico, Journal of Iberian Geology, 48, 461–486, https://doi.org/10.1007/s41513-022-00201-7, 2022.

Verma, S. P., Pandarinath, K., Verma, S. K., and Agrawal, S.: Fifteen new discriminant-function-based multi-dimensional robust diagrams for acid rocks and their application to Precambrian rocks, Lithos, 168, 113–123, https://doi.org/10.1016/j.lithos.2013.01.014, 2013.

Vigneresse, J. L.: The specific case of the Mid-Proterozoic rapakivi granites and associated suite within the context of the Columbia supercontinent, Precambrian research, 137, 1–34, https://doi.org/10.1016/j.precamres.2005.01.001, 2005.

Wang, C., Mitchell, R. N., Murphy, J. B., Peng, P., and Spencer, C. J.: The Role of Megacontinents in the Supercontinent Cycle, Geology, 49, 402–406, https://doi.org/10.1130/G47988.1, 2020.

Ward, Joe H., J.: Hierarchical Grouping to Optimize an Objective Function, Journal of the American Statistical Association, 58, 236–244, https://doi.org/10.1080/01621459.1963.10500845, 1963.

https://doi.org/10.5194/egusphere-2026-4451
Preprint. Discussion started: 22 September 2026

Whalen, J. B., Currie, K. L., and Chappell, B. W.: A-type granites: geochemical characteristics, discrimination and petrogenesis, Contributions to Mineralogy and Petrology, 95, 407–419, https://doi.org/10.1007/BF00402202, 1987.

Yang, X.-M.: Estimation of crystallization pressure of granite intrusions, Lithos, 286, 324–329, https://doi.org/10.1016/j.lithos.2017.06.018, 2017.

Yang, X.-M., Lentz, D. R., and Chi, G.: Ferric-ferrous iron oxide ratios: Effect on crystallization pressure of granites estimated by Qtz-geobarometry, Lithos, 380, 105 920, https://doi.org/10.1016/j.lithos.2020.105920, 2021.